

Classical, large scale 3D MHD simulations of interacting pulsar wind nebulae

D. M.-A. Meyer¹ and D. F. Torres^{1,2,3}

¹ Institute of Space Sciences (ICE, CSIC), Campus UAB, Carrer de Can Magrans s/n, 08193 Barcelona, Spain
e-mail: meyer@ice.csic.es ; dmameyer.astro@gmail.com

² Institut d'Estudis Espacials de Catalunya (IEEC), 08034 Barcelona, Spain
e-mail: dtorres@ice.csic.es

³ Institució Catalana de Recerca i Estudis Avançats (ICREA), 08010 Barcelona, Spain

ABSTRACT

Context. Magnetized rotating neutron stars, or pulsars, are a possible end product of massive star evolution. Their relativistic wind successively interacts with the supernova ejecta of their defunct progenitor, then with the circumstellar medium of the progenitor, and eventually with the interstellar medium. The distribution of those materials governs the morphology, mixing of chemical elements, and emission properties of the shocks present in plerionic supernova remnants.

Aims. If a massive star is static with respect to its ambient medium, then its resulting circumstellar medium is elongated along the direction of the local magnetic field, and its supernova remnant transiently appears as a rectangle. The pulsar wind nebula forming in it, in its turn, elongated, as long as the pulsar's axis of rotation matches the direction of the local magnetization. In this work, we explore how the angle between the direction of the local magnetic field of the interstellar medium and the pulsar axis of rotation influences the shaping of its pulsar wind nebula.

Methods. Three-dimensional magneto-hydrodynamic simulations are carried out with the PLUTO code to model the pulsar wind nebula formed by a static pulsar inside of a supernova remnant left behind by a massive Wolf-Rayet-evolving progenitor at rest in an organized, magnetized ambient medium. We use those models to perform radiative transfer calculations to derive non-thermal radio emission maps of the pulsar wind nebulae.

Results. When the polar elongation of the pulsar develop, they bend in opposite directions under the effects of the cavity carved by the stellar wind and already filled by supernova ejecta. This induces a complex distribution of magnetized supernova ejecta and pulsar wind, resulting in various observable structures, appearing as rectangles, circles, or irregular oblong shapes, in the radio waveband.

Conclusions. The angle between the direction of the pulsar rotation axis and that of the local ambient magnetization is a governing parameter for the shaping and non-thermal radio properties of the pulsar wind nebulae of static massive stars; however, the mixing of material, once the pulsar wind nebula is old (50–80 kyr), is not strongly affected by that factor.

Key words. methods: MHD – stars: evolution – stars: massive – pulsars: general – ISM: supernova remnants.

1. Introduction

Pulsars are highly magnetized, rotating neutron stars formed from the explosive deaths of massive stars, provided the collapse does not directly result in a black hole (Gold 1968; Pacini 1968; Lyne & Graham-Smith 2012). Their magnetized surfaces launch powerful relativistic winds, which interact with the surrounding environment to produce pulsar wind nebulae, as reviewed in Gaensler & Slane (2006); Kargaltsev et al. (2017a); Olmi & Bucciantini (2023). These nebulae emit across the entire electromagnetic spectrum, with synchrotron radiation and inverse Compton scattering dominating their non-thermal emission (Kennel & Coroniti 1984; Gaensler & Slane 2006). Additional features include distinct emission lines (Reynolds et al. 2017), as well as observational signatures in the radio band (e.g., G54.1+0.3 (Driessen et al. 2018)), X-rays (e.g., G11.2–0.3 (Borkowski et al. 2016)), and gamma-rays extending to PeV energies, notably in the Crab Nebula (Aharonian et al. 2006; Abdalla et al. 2021; Lhaaso Collaboration et al. 2021; Acero et al. 2023). The morphology and dynamical evolution of pulsar wind nebulae are significantly shaped by their surrounding medium, whether confined within progenitor supernova remnants or propagating through the interstellar medium

(ISM) as bow shocks, following the natal kicks imparted to pulsars (Temim et al. 2015). The interaction between pulsar winds and the dense, anisotropic ejecta of core-collapse supernovae can generate complex structures and irregular emission features (Reynolds et al. 2017; Olmi & Bucciantini 2023). Comprehensive catalogues of observed pulsar wind nebulae have been assembled in multiple studies (Hester 2008; Bühler & Blandford 2014; Bock et al. 1998; Kargaltsev & Pavlov 2007; Kargaltsev et al. 2012, 2017b; Frail & Scharringhausen 1997; H. E. S. S. Collaboration et al. 2018; Popov et al. 2019; H. E. S. S. Collaboration et al. 2019; Acero et al. 2023; Turner et al. 2024).

Pulsar wind nebulae are extreme environments that can only be effectively probed through numerical simulations. The body of literature on simulations of pulsar wind nebulae generally divides into two main groups of studies. On the one hand, there are models focusing on the immediate surroundings of the pulsar and tracking the evolution of the nebula up to timescales of approximately 1 kyr after the onset of the pulsar wind (Kennel & Coroniti 1984; Coroniti 1990; Begelman & Li 1992; Begelman 1998; Komissarov & Lyubarsky 2003; van der Swaluw et al. 2003; Komissarov & Lyubarsky 2004; van der Swaluw et al. 2004; Komissarov 2006; Del Zanna et al. 2006; Camus

et al. 2009; Komissarov & Lyutikov 2011; Olmi et al. 2014; Porth et al. 2014; Olmi et al. 2016). On the other hand, there are simulations that encompass the entire circumstellar medium and the supernova ejecta, extending to about 30 kyr after the explosion (Temim et al. 2015, 2017; Kolb et al. 2017; Temim et al. 2022), or tracking the nebula as it moves through the ISM after being expelled from its parent supernova remnant (Bucciantini & Bandiera 2001; Bucciantini 2018; Barkov & Bosch-Ramon 2018; Barkov et al. 2019a,b; Toropina et al. 2019; Olmi & Bucciantini 2019a,b,c). Among the various factors influencing the morphology of pulsar wind nebulae, the interaction of the progenitor’s stellar winds plays a dominant role in shaping their structure and emission properties (Meyer & Meliani 2022; Meyer & Torres 2025; Meyer et al. 2025).

The circumstellar medium of massive stars is commonly described by the stellar wind bubble model (Weaver et al. 1977). This model envisions the stellar surroundings as a series of shocks and discontinuities, bounded by an inner termination shock and an outer forward shock. Within this structure, concentric and often unstable layers of hot, diluted gas and cold, dense stellar wind material form. Wind bubbles are influenced by several factors, including the bulk motion of the central massive star, which can transform the circumstellar medium into a stellar wind bow shock (Gull & Sofia 1979; Wilkin 1996), stellar rotation, and the granularity of the multi-phase ambient medium (McKee & Ostriker 1977). The circumstellar medium is continuously reshaped by the stellar feedback from its central star. Regular variations in the stellar wind, which mark the transition between different evolutionary phases following the long initial main-sequence stage, further modify the internal regions of the circumstellar medium in terms of momentum and chemical composition. This evolution gives rise to structures associated with red supergiants (Noriega-Crespo et al. 1997; Decin et al. 2012) or luminous blue variables (González & Koenigsberger 2014). At the end of the star’s life, the supernova blast wave interacts with the pre-shaped circumstellar medium, generating a supernova remnant whose properties reflect the evolutionary history of its progenitor (Weiler & Shaver 1978; Caswell 1979; Weiler & Panagia 1980; Gaensler & Slane 2006; Kargaltsev et al. 2017a).

The influence of the magnetic field in the ISM on the morphology of circumstellar nebulae is well-studied. It serves as a stabilizing mechanism for the instabilities of stellar wind bow shocks from massive runaway stars (Meyer et al. 2017; Baalman et al. 2021; Meyer et al. 2021a), elongates the shapes of stellar wind bubble and superbubbles (van Marle et al. 2015) along the direction of the local ambient magnetic field. After the explosive death of massive progenitor stars, their magnetized circumstellar medium presents an obstacle to the expanding supernova blastwave (Langer 2012; Orlando et al. 2019, 2020, 2021, 2022, 2025). This interaction can result in an asymmetric supernova remnant (Meyer et al. 2021b), modify the mixing of the ejecta with surrounding ISM material (Meyer et al. 2023), and influence phenomena such as non-thermal emission (Meyer et al. 2024b).

About a third of massive stars, i.e. of core-collapse supernova progenitors, move supersonically through the ISM (de Wit et al. 2005) and generate a dense stellar wind bow shock (van Buren et al. 1995) which strongly affects the propagation of the supernova blastwave (Meyer et al. 2015). We have investigated the scenario of a young pulsar in such supernova remnant in Meyer et al. (2025). In the case of a static supernova progenitor, the reflection of the supernova blastwave off the walls of the oblong cavity generates a tubular structure, which appears as a rectan-

gle in projected emission (Meyer et al. 2022) and notable examples of such objects include the supernova remnant Puppis A. As demonstrated in previous studies, the morphology of pulsar wind nebulae originating from massive progenitors is also influenced by the local distribution of ejecta, stellar wind, and ISM. Consequently, the pulsar wind nebulae of static massive progenitors are stretched along the direction of the ISM’s magnetic field (Meyer et al. 2024a).

The two-dimensional nature of the models in Meyer et al. (2024a) obliged us to consider colinear directions for both the ISM magnetic field and the axis of rotation of the pulsar. In this work, we extend these numerical efforts by presenting 3D MHD simulations of the pulsar wind nebula of a static massive star. The effects of the magnetization of the ISM on the elongation of its progenitor’s circumstellar medium at the pre-supernova time are included, and we present non-thermal radio emission maps of our results. In Section 2, we present the methods used in this study; in Section 3, we detail the obtained results, which are further discussed in Section 4. We draw our conclusions in Section 5.

2. Method

2.1. Simulation strategy

In this study, we perform a series of global simulations for the pulsar wind nebulae of a static massive star. The models are carried out within the framework of classical magnetohydrodynamics using the PLUTO code (Mignone et al. 2007, 2012).

Since the circumstellar medium of massive stars governs the morphology and various properties of supernova remnants, and, through density wave reflections, it also influences the pulsar wind nebulae forming in the relics of core-collapse supernovae, our model covers the entire evolution of the surroundings of the massive progenitor, from the zero-age main-sequence phase up to 80 kyr after the supernova explosion. First, the circumstellar medium, produced by the interaction of the massive star’s stellar wind with the ISM, is modeled throughout the star’s entire life. It is simulated in 2.5D, using a cylindrical coordinate system (2D for scalar quantities plus a toroidal component for the vectors), in the frame of the static star, to be used as initial conditions for the supernova remnant phase calculation (Meyer et al. 2025). Secondly, the interaction of the supernova blast wave with the freely-expanding stellar wind from the progenitor’s last evolutionary phase is modeled in a 1D spherical coordinate system until its forward shock reaches a distance of 2 pc, smaller than the termination shock of the stellar wind bubble. Thirdly, a 3D Cartesian simulation is performed, using the 2.5D circumstellar medium that is rotated around its symmetry axis to reconstruct a 3D structure. The 1D solution is then mapped onto this 3D structure, assuming an isotropic supernova explosion, providing the initial conditions for the global plerionic supernova remnant models. This study focuses on pulsar wind nebulae which are interacting with their pre-supernova circumstellar medium, and, on the associated aftermaths of it. In the warm phase of the ISM, this corresponds to older plerion (≥ 40 kyr), see Meyer et al. (2024a). The workflow is summarised in Fig. A.1.

2.2. Interstellar medium

The single massive star considered in this study is assumed to reside in a uniform medium that mimics the plane of the Milky Way, specifically in the warm phase of the ISM. Its temperature is set to $T_{\text{ISM}} = 8000$ K, with a number density of

$n_{\text{ISM}} = 0.79 \text{ cm}^{-3}$ and a magnetic field strength of $B_{\text{ISM}} = 7 \mu\text{G}$ (Wolfire et al. 2003; Meyer et al. 2024b). The ISM is assumed to be in equilibrium with optically-thin radiative processes for cooling and heating. Coolants from elements such as H, He, and metals (at solar He abundance) are included, following the prescriptions of Wiersma et al. (2009); Asplund et al. (2009). Additionally, our model incorporates contributions from H recombination lines (Hummer 1994), as well as emission from forbidden lines of O and C (Henney et al. 2009). Cooling by O is particularly important for shock physics, and it is assumed to be present in the ISM at an abundance of $\text{O}/\text{H} = 4.89 \times 10^{-4}$ in number density, as presented by Asplund et al. (2009). Starlight heating, through the recombination of hydrogenic ions ionized by stellar irradiation, is included as described in Osterbrock & Bochkarev (1989). The background magnetic field initially filling the ISM is uniform and linearly organized, which is consistent with the large scale coherent magnetic fields observed in the Galactic spiral arms of the Milky Way (Rand & Kulkarni 1989). Since the circumstellar medium of the massive star is modeled in two dimensions, it forces to adopt the configuration of a runaway progenitor moving parallel to the magnetic field lines of the local ambient medium, see Meyer et al. (2017).

2.3. Stellar wind interaction with the ambient medium

The interaction of the stellar wind with the ISM is simulated by placing a $35 M_{\odot}$ static star for which the time-dependent stellar surface properties, namely the mass-loss rate, the wind velocity, the effective temperature are taken from the GENEVA library of evolutionary track (Ekström et al. 2012). The value of the star terminal wind speed is calculated from the stellar escape velocity using the recipe of Eldridge et al. (2006). The stellar rotation is selected to be $\Omega_{\star}(t=0)/\Omega_{\text{K}} = 0.1$ with $\Omega_{\star}(t=0)$ and Ω_{K} the zero-age main-sequence rotational velocity at the equator and the Keplerian rotational speed, respectively. This permits to include both the latitude-dependent toroidal component of the stellar rotation in the spirit of Parker (1958); Weber & Davis (1967); Chevalier & Luo (1994); Rozyczka & Franco (1996); Pogorelov & Semenov (1997); Pogorelov & Matsuda (2000). The stellar magnetic field structure is assumed to be a Parker spiral with a magnetic field strength at the surface scaled as the Sun's one (Scherer et al. 2020; Herbst et al. 2020; Baalman et al. 2020, 2021; Meyer et al. 2021a) and which value is $B_{\star} = 500 \text{ G}$ (Fossati et al. 2015; Castro et al. 2015), $B_{\star} = 0.2 \text{ G}$ (Vlemmings et al. 2002, 2005) and $B_{\star} = 100 \text{ G}$ (Meyer 2021) for the main-sequence, red supergiant and Wolf-Rayet phases, respectively. The simulation of the CSM surrounding the massive star is performed using a 2.5D cylindrical coordinate system. It employs a uniform grid covering the range $[0, 150] \times [-50, 50] \text{ pc}$ consisting of 7500×5000 or a uniform spatial resolution of $0.02 \text{ pc zone}^{-1}$.

2.4. Supernova blastwave interaction with the stellar wind

The supernova blast wave resulting from the explosion is simulated using a 1D spherically symmetric coordinate system, extending to a maximum radius of $r_{\text{max}} = 2 \text{ pc}$. During this initial phase, the shock front propagates through the freely expanding stellar wind, which is assumed to be isotropic. The numerical grid consists of 50000 uniformly spaced zones, providing sufficient resolution to accurately capture the shock dynamics. The core-collapse supernova explosion model adopted in this study follows the prescriptions of Whalen et al. (2008), van Veelen et al. (2009), and Truelove & McKee (1999). The total ejected

mass is set to $M_{\text{ej}} = 10.12 M_{\odot}$, obtained by subtracting the neutron star mass of $1.4 M_{\odot}$ from the progenitor's final stellar mass at the time of core collapse. The explosion is assumed to release a total energy of $E_{\text{ej}} = 10^{51} \text{ erg}$. When the forward shock of the expanding supernova blast wave reaches a radius of 1.2 pc from the center of the explosion, the simulation transitions to a 3D Cartesian coordinate system spanning a domain of $[-50, 50]^3 \text{ pc}$. This computational grid consists of 2048^3 uniformly spaced zones. The initial conditions for this phase include the circumstellar medium at the pre-supernova stage, reconstructed from the previously described 2.5D simulation under the assumption of rotational symmetry. The angle θ_{mag} , defined as the angle between the symmetry axis of the circumstellar medium (aligned with the progenitor's motion) and the Oz axis of the Cartesian grid, is treated as a free parameter in this study.

2.5. Pulsar wind interaction with the supernova ejecta

Following the core-collapse supernova explosion, the emergence of the pulsar wind is introduced after a delay of approximately 20 yr , corresponding to the free expansion phase of the remnant. The wind is injected isotropically within a spherical region of radius 0.4 pc under non-relativistic conditions, following the method of Komissarov & Lyubarsky (2004). Although this simplification omits relativistic corrections, it provides a numerically stable and physically consistent framework for capturing the large-scale interaction between the pulsar wind and the surrounding supernova ejecta (Del Zanna et al. 2006). We adopt a single ideal-gas equation of state throughout the computational domain with adiabatic index $\gamma = 5/3$, which is a common simplification in global modelling of composite supernova remnants, although the material of the pulsar wind is expected to behave closer to a relativistic gas of adiabatic index $\gamma = 4/3$. Using $\gamma = 5/3$ instead of $\gamma = 4/3$ increases the gas pressure by a factor of ≈ 2 , which can mildly bias the effective expansion of the nebula, its morphological and emission properties. Our work focuses on the large scale shaping by the pre-supernova circumstellar cavity, the motion of the progenitor star and the ISM magnetization, we do not expect this approximation to qualitatively modify the trends reported in this work.

The pulsar is initialized with an initial spin period of $P_0 = 0.3 \text{ s}$ and a spin-down rate $\dot{P}_0 = 10^{-17} \text{ s s}^{-1}$, under the standard assumption of a braking index $n = 3$, indicative of magnetic dipole radiation. This yields a spin-down luminosity of $\dot{E}_0 = 10^{38} \text{ erg s}^{-1}$ at the onset of the pulsar wind nebula phase. Following Komissarov & Lyubarsky (2004), we inject a magnetised wind that is initially made of a purely toroidal component with a polar dependence that is symmetric in geometry across the equator. The velocity of the injected wind is taken to be $0.01c$, where c is the speed of light. Although this is sub-relativistic, it remains sufficient to produce the expected expansion behavior of young plerions. Such pulsar properties are taken from Slane (2017) and have been used in Meyer et al. (2025). Hence, this study does not consider yet the pulsar properties as free parameters; which could potentially affect the results. For instance, a less luminous pulsar will inefficiently prevent the reflection of the supernova blastwave and generate, at similar time after the explosion, a smaller nebula.

The magnetization parameter is set to $\sigma = 10^{-3}$. This choice prioritizes numerical robustness in these global, long-term ($\geq 50\text{--}80 \text{ kyr}$) multi-dimensional runs, and limits sensitivity to resolution-dependent in the region near the pulsar wind termination shock and in the other strongly magnetized shear layers of the supernova remnant. Note that $\sigma \geq 10^{-2}$ is often re-

quired in axisymmetric (and some 3D) studies to obtain magnetically collimated, hoop-stress-driven polar elongations in the inner nebula (Del Zanna et al. 2004; Bucciantini et al. 2004; Porth et al. 2014). This work does not aim to reproduce that inner jet-launching regime, and, the bipolar structures we refer to in the discussion below relate to large scale polar outflows guided by the cavity geometry and the total pressure distribution.

We assume a symmetric explosion, such that the neutron star remains fixed at the center of the computational domain. Its rotation axis is aligned with the O_z direction of the 3D Cartesian grid, which facilitates a clean exploration of the impact of the misalignment between the ISM magnetic field and the pulsar’s spin axis. This angle, θ_{mag} , is varied in the simulations to investigate its effect on the shape, structure, and emission properties of the resulting plerion.

2.6. Emission maps

In order to directly compare the numerical models of pulsar wind nebulae developed in this study with real astronomical observations, non-thermal emission maps in the radio waveband are generated. These maps provide insight into the spatial distribution and intensity of synchrotron radiation emitted by non-thermal electrons interacting with the magnetic field within the plerion. The calculations are carried out using the radiative transfer code RADMC-3D (Dullemond 2012), which allows for detailed modeling of radiation processes in astrophysical environments. The methodology used to compute the synchrotron emission coefficients, which quantify the amount of radiation produced per unit volume, follows the approach described in Meyer et al. (2021b). This procedure accounts for both the energy distribution of relativistic electrons and the local magnetic field strength and structure. The method is based on the formalism outlined in Villagran et al. (2024) and Meyer et al. (2024b). To produce the intensity maps, the computed emissivity distribution is projected onto the plane of the sky, considering the inclination angle of the supernova remnant relative to the observer’s line of sight. Because the dynamics are computed in the non-relativistic magneto-hydrodynamics approximation and we do not apply the Doppler boosting or any aberration corrections in the post-processing, the synthetic maps are intended for qualitative discussion of the large-scale morphology at this stage, rather than for a detailed test of the asymmetries of the brightnesses of the inner nebula.

2.7. Numerical methods

To ensure the fidelity of the interaction between the pulsar wind and the interstellar medium when simulating the evolution of the pulsar wind nebula, the computational grid for the circumstellar medium is assigned a spatial resolution exceeding that of the plerionic supernova remnant. This refinement guarantees that the termination shock of the pulsar’s wind nebula is sufficiently resolved, mitigating numerical boundary effects that could otherwise introduce artificial structures. The numerical framework is constructed upon a dimensionally unsplit, finite-volume solver based on the Godunov method. The system integrates the Harten–Lax–van Leer approximate Riemann solver (Harten et al. 1983) for flux computations, coupled with a third-order Runge–Kutta temporal integration scheme. Reconstruction of primitive variables between adjacent computational cells follows a hybrid methodology: the circumstellar medium employs a piecewise parabolic method to enhance accuracy, whereas the

supernova remnant is computed using a linear reconstruction scheme constrained by a minmod slope limiter. The latter approach enforces a total variation diminishing condition, preserving numerical stability in regions exhibiting steep gradients. Temporal evolution adheres to the Courant–Friedrichs–Levy condition, which is initially defined by a number of 0.3 to maintain stability while maximizing computational efficiency. Furthermore, divergence-free preservation of the magnetic field vector throughout the domain is enforced through the divergence-cleaning methodology of Powell (Powell 1997), ensuring compliance with the solenoidal constraint in magnetohydrodynamic simulations.

3. Results

3.1. Effects of the magnetic field direction on the properties of the supernova remnants

Fig. 1 shows the number density fields in 3D plerionic supernova remnant models of a static $35 M_{\odot}$ star rotating at an equatorial rate of $\Omega_{\star}/\Omega_K = 0.1$. This baseline model represents a supernova remnant and its pulsar wind nebula evolving in an ISM with a magnetic field of strength $B_{\text{ISM}} = 7 \mu\text{G}$, aligned with the O_z axis of the Cartesian coordinate system—which, in this case, also corresponds to the rotation axis of the pulsar. The panels display slices of the number density field in the $z = 0$ (Fig. 1a), $y = 0$ (Fig. 1b), and $x = 0$ (Fig. 1c) planes, taken at 50 kyr after the onset of the supernova explosion. The different contours indicate regions of the supernova remnant with a 50% number density contribution from the pulsar wind (black) and the supernova ejecta (cyan), as well as a 10% contribution from Wolf–Rayet (magenta) and red supergiant wind (red) material. The cavity carved out during the progenitor’s lifetime is bounded by the termination shock of the stellar wind bubble, which is elongated along the direction of the ISM magnetic field (van Marle et al. 2015). This cavity appears tubular due to the 2.5-dimensional nature of the circumstellar medium simulation (Meyer et al. 2024b) (see Fig. 1a), allowing the formation of a pulsar wind nebula composed of an equatorial disc and a polar elongation extending up to ± 25 pc along the O_z direction, rather than exhibiting the diamond-like morphology described by Komissarov & Lyubarsky (2004).

Figs. B.1 and B.2 are similar to Fig. 1, with angles $\theta_{\text{mag}} = 30^\circ$ and $\theta_{\text{mag}} = 45^\circ$ between the local ISM field and the pulsar rotation axis, respectively. The intersections of the tubular cavity of stellar wind, in which the supernova ejecta and the pulsar wind were released and evolved, with the $z = 0$ and $y = 0$ planes are ellipses (Figs. B.1a,b and B.2a,b). In contrast, the intersection with the $x = 0$ plane corresponds to the same tubular cavity as in Fig. 1b,c, rotated by angles $\theta_{\text{mag}} = 30^\circ$ and $\theta_{\text{mag}} = 45^\circ$, respectively. The morphology of the pulsar wind nebula is strongly influenced by the direction of the cavity in which the material can freely expand. Specifically, the disc no longer lies in the equatorial plane of the rotating pulsar; instead, it grows in a plane that forms an angle θ_{mag} with the $z = 0$ plane. With more space available, as it is no longer confined by the walls of the stellar wind cavity (see Fig. 1b,c), the pulsar wind nebula disc is larger and extends to distances twice that of the model with $\theta_{\text{mag}} = 0^\circ$. Similarly, the polar elongations of the pulsar wind are affected by the distribution of circumstellar material and bend due to the ram pressure exerted by the defunct stellar wind and the supernova ejecta reflecting within the cavity. This pressure compresses the polar elongation and channels it towards the end of the cavity, naturally producing a complex shape with a wobbled disc and a

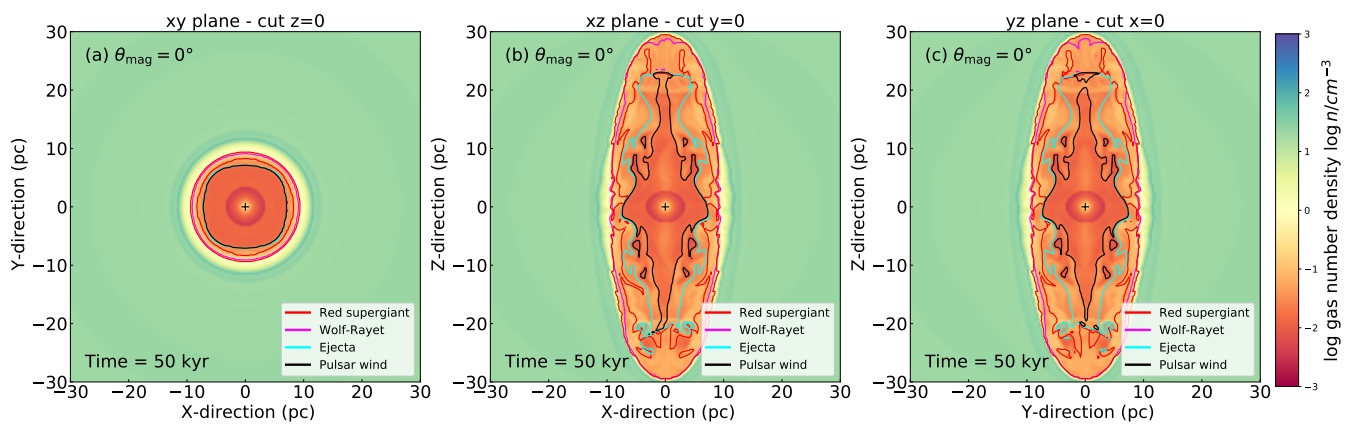


Fig. 1. The number density fields in the 3D supernova remnant models of a static $35 M_{\odot}$ star rotating with $\Omega_{\star}/\Omega_K = 0.1$. The ISM magnetic field is aligned with the Oz Cartesian axis and has a strength of $B_{\text{ISM}} = 7 \mu\text{G}$. The figures show the supernova remnant in the $z = 0$ (left), $y = 0$ (middle), and $x = 0$ (right) planes of the Cartesian coordinate system, at 50 kyr after the onset of the explosion. The results are shown for an angle $\theta_{\text{mag}} = 0^{\circ}$ between the pulsar’s rotation axis and the direction of the local ISM. The different contours indicate regions of the supernova remnant with a 50% contribution from pulsar wind (black) and ejecta (cyan), as well as regions with a 10% contribution from Wolf–Rayet (magenta) and red supergiant wind (red) material, respectively. The black cross marks the position of the supernova explosion.

bent bipolar structure. The outer extent of the bipolar structure realigns with the direction of the local ISM magnetic field (see Fig. B.1c).

Finally, Fig. B.3 presents the pulsar wind nebula modeled with $\theta_{\text{mag}} = 90^{\circ}$. The intersection of the circumstellar medium with the $x = 0$ plane appears as a circle and shares the same elongated cavity shape as shown in Fig. 1 for the other planes. The morphology of the pulsar wind nebula exhibits an equatorial disc that is significantly more extended than the polar elongation originating from it (Fig. B.3a). This configuration results from the orientation of the circumstellar medium, which is influenced by the direction of the local magnetization of the ISM. The diamond-shaped structure identified in the study by Komissarov & Lyubarsky (2004) reappears; however, the two components of the polar elongation are thicker and less affected by instabilities. Additionally, the space occupied by the disc adopts a rectangular morphology with protuberances along the y -axis direction (Meyer et al. 2024a), as depicted in Fig. B.3ac.

3.2. Time evolution of the plerionic supernova remnant

Fig. 2 shows the time evolution of the pulsar wind nebula with $\theta_{\text{mag}} = 0^{\circ}$, from 40 kyr (Fig. 2a) to 80 kyr (Fig. 2c) after the supernova explosion, as shown in the $x = 0$ plane. The disc of the pulsar wind nebula grows along the Ox direction. It has been demonstrated that the supernova shock wave reflects off the walls of the stellar wind cavity, and that a wave propagates back to the explosion center, inducing the formation of rectangular supernova remnants (Meyer et al. 2022). Additionally, the release of a pulsar wind after the explosion further shapes the plerion (Meyer et al. 2024a). In this scenario, the pulsar wind, initially stretched along Oy but relatively compact along Ox , interacts with the reflected waves of the forward shock that has impacted the termination shock of the supernova blastwave (Fig. 2a,b). A similar phenomenon occurs with the polar elongation interacting with the end of the circumstellar cavity previously filled with ejecta. This interaction leads to the detachment of clumps rich in pulsar wind material, resulting in a smaller, denser pulsar wind nebula. Consequently, the disc-to-polar elongation size ratio becomes larger compared to earlier evolutionary phases (Fig. 2c).

Fig. C.1a depicts the simulation with $\theta_{\text{mag}} = 30^{\circ}$, where the misalignment between the pulsar’s equatorial plane and either the equatorial plane of the pulsar wind nebula or the direction of the polar elongations—both channeled through the low-density region of stellar wind—is evident at 40 kyr post-explosion, persisting thereafter (Fig. C.1b,c). As time progresses, the pulsar wind nebula’s morphology becomes increasingly distorted, adopting the shape of a complex region with a squared core and arms emerging from its edges, particularly distorted at the bottom of the circumstellar cavity by 80 kyr (Fig. C.1c). In the model with $\theta_{\text{mag}} = 45^{\circ}$, the angle between the pulsar’s rotation axis and the local interstellar medium (ISM) magnetic field direction reduces the alignment between the disc and the polar elongation. At 40 kyr, the polar elongation splits into two smaller filaments (Fig. C.2a), which merge into a single structure by 50 kyr (Fig. C.2b). By 80 kyr, this evolves into a central squared structure with two thick polar elongations attached, forming a complex pulsar wind nebula (Fig. C.2c).

Fig. C.3a illustrates the time evolution of the pulsar wind nebula for $\theta_{\text{mag}} = 90^{\circ}$. At 40 kyr, the disc aligns with the pulsar’s rotation plane, extending farther than the polar elongation. Here, the equatorial plane interacts with the end of the circumstellar cavity, becoming unstable and diminishing in size due to reflections from both the pulsar wind’s forward shock and the supernova blastwave’s forward shock. The polar elongation evolves as it first impacts the cavity, enlarging the filaments perpendicular to the equatorial disc by 50 kyr (Fig. C.3b). The system continues to evolve, adopting a squared shape with several polar elongations and filaments emerging by 80 kyr (Fig. C.3c).

3.3. Structure of the pulsar magnetic field

Fig. 3 displays volumetric renderings of the 3D MHD models for pulsar wind nebulae and their complex environments. The colour coding is as follows. The orange surfaces mark regions of constant density stellar wind material and therefore highlight the location of the stellar wind bubble shaped by the progenitor prior to the explosion. The red surface trace the red supergiant wind in 10% in number density, the magenta surface traces the Wolf-Rayet in 10% in number density, the cyan surface traces the the locations of the supernova ejecta being 50% in number density and the white tubes trace the magnetic field lines of the

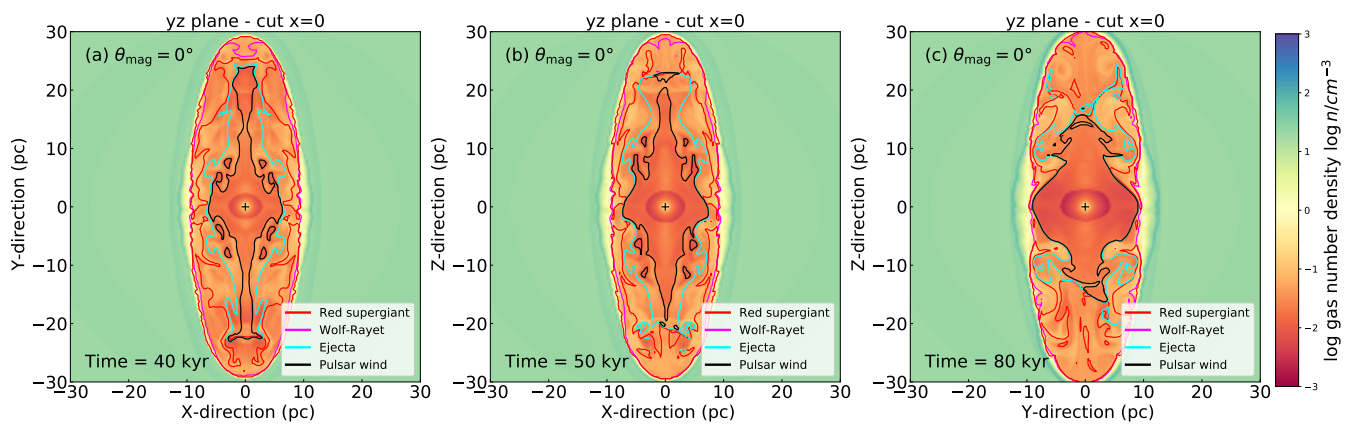


Fig. 2. Time evolution of the number density fields in the 3D supernova remnant models of a static $35 M_{\odot}$ star rotating with $\Omega_{\star}/\Omega_{\text{K}} = 0.1$. The ISM magnetic field is aligned with the Oz Cartesian axis and has a strength of $B_{\text{ISM}} = 7 \mu\text{G}$. The figures show the supernova remnant in the $z = 0$ (left), $y = 0$ (middle), and $x = 0$ (right) planes of the Cartesian coordinate system, spanning times from 40 kyr to 80 kyr after the onset of the explosion. The results are shown for an angle $\theta_{\text{mag}} = 0^{\circ}$ between the pulsar’s rotation axis and the direction of the local ISM. The different contours indicate regions of the supernova remnant with a 50% contribution from pulsar wind (black), ejecta (cyan), Wolf–Rayet (magenta), and red supergiant wind (red) material, respectively. The black cross marks the position of the supernova explosion.

pulsar wind. The displayed models differ by the angle between the ISM magnetic field lines shaping the main-sequence stellar wind bubble (orange) and the axis of rotation of the pulsar (fixed in all models as being along the vertical direction). The angle is of $\theta_{\text{mag}} = 0^{\circ}$ (a), $\theta_{\text{mag}} = 30^{\circ}$ (b), $\theta_{\text{mag}} = 45^{\circ}$ (c) and $\theta_{\text{mag}} = 90^{\circ}$ (d), respectively. Fig. 4 additionally shows the distribution of the toroidal to total magnetic field ratio B_{ϕ}/B , with arrows tracing the magnetic field vectors in the yOz plane for the regions of the supernova remnant and contours highlighting the contact discontinuities of the several materials mixing into the remnant.

In Figure 3a, with $\theta_{\text{mag}} = 0^{\circ}$, the large-scale circumstellar wind bubble extends over a spherical region with a radius of approximately 30 pc. The density surface highlights the outer forward shock of the wind bubble, which is axisymmetric due to its pre-calculation in 2.5 dimensions. This configuration results in an increase in density, forming oblate shells stretched along the pulsar’s rotation axis, aligning with the local ISM magnetic field direction. The concentrations of isodensity surfaces denote the region of the termination shock of the stellar wind cavity, which has been impacted by the forward shock of the supernova blastwave. Inside this cavity, the red supergiant material has dispersed throughout the available space, propelled by the last pre-supernova stellar wind expelled during the Wolf-Rayet evolutionary phase. The supernova ejecta fill the entire cavity, mixing with other materials. The distribution of magnetic field lines exhibits the typical morphology of a toroidal field, wrapping around the central pulsar and being displaced by its wind. The region of unmixed pulsar wind (black contour) is dominated by a toroidal field, except at the apex of its bipolar elongations. In the extends of the cavity, where ejecta and stellar wind meet, the magnetic field is disorganised (Fig. 4a). The pulsar wind predominantly occupies the central spherical region where the supernova blastwave first interacted with the stellar wind cavity.

Figs. 3b,c show the plerionic supernova remnant for $\theta_{\text{mag}} = 30^{\circ}$ and $\theta_{\text{mag}} = 45^{\circ}$, respectively, where the location of the cavity is no longer aligned with the pulsar rotation axis. This has the following effect: the distribution of the magnetic field lines loses symmetry but propagates towards the end of the cavity, where they reconnect, forming a complex interlace that strongly deviates from the situation with $\theta_{\text{mag}} = 0^{\circ}$ (Fig. 3a). The same occurs in the model with $\theta_{\text{mag}} = 45^{\circ}$ (Fig. 3c). Fig. 3d illustrates the

simulation with $\theta_{\text{mag}} = 90^{\circ}$ in which the pulsar rotation axis is normal to the direction of the local magnetic field. The toroidal component of the pulsar wind magnetosphere extends deep into the cavity, whereas the polar elongation hits its walls and thickens the polar region towards the disc. The bouncing mixed material of ejecta and stellar wind can be locally organised towards the center of the stretched cavity, although mostly made of a poloidal magnetic field (Fig. 4b).

Fig. 5 is similar to Fig. 3, showing the volumetric rendering of the supernova ejecta (cyan surfaces) and the pulsar wind magnetic field lines (white tubes). The toroidal structure of the magnetic fields wraps around the contact discontinuity between the supernova ejecta and pulsar wind material, extending up to the end of the stellar wind cavity, which is normal to the pulsar equatorial plane, as shown in Fig. 5a. When an angle $\theta_{\text{mag}} = 30^{\circ}$ is introduced between the direction of the pulsar rotation axis and the local ISM magnetic field direction, the distribution of the pulsar wind magnetic field lines changes accordingly. These field lines wrap around the contact discontinuity of the supernova ejecta, while maintaining their local toroidal direction, reconnecting with the ISM magnetic field that has penetrated the post-shock region of the circumstellar wind bubble and borders the edge of the stellar wind cavity. The field lines are particularly disorganized at the end of the cavity, where the region is more turbulent and hosts a lot of mixing of materials (Fig. 5b). A similar situation occurs in the model with $\theta_{\text{mag}} = 45^{\circ}$ (Fig. 5c). The situation with $\theta_{\text{mag}} = 90^{\circ}$ resembles that with $\theta_{\text{mag}} = 0^{\circ}$ except that the toroidal field lines wrap around the entire contact discontinuity of the supernova ejecta, which is aligned with the pulsar equatorial plane (Fig. 5d). Both the vicinity of the pulsar as well the regions close to the discontinuities where a lot of mixing happens are filled with toroidally magnetised material, while the bouncing supernova ejecta are mostly poloidally magnetised (Fig. 4d).

4. Discussion

4.1. Limitations of the models

The limitations of the simulations presented in this paper are threefold. First, the axisymmetric nature of the circumstellar medium used as initial conditions for the pulsar wind nebula

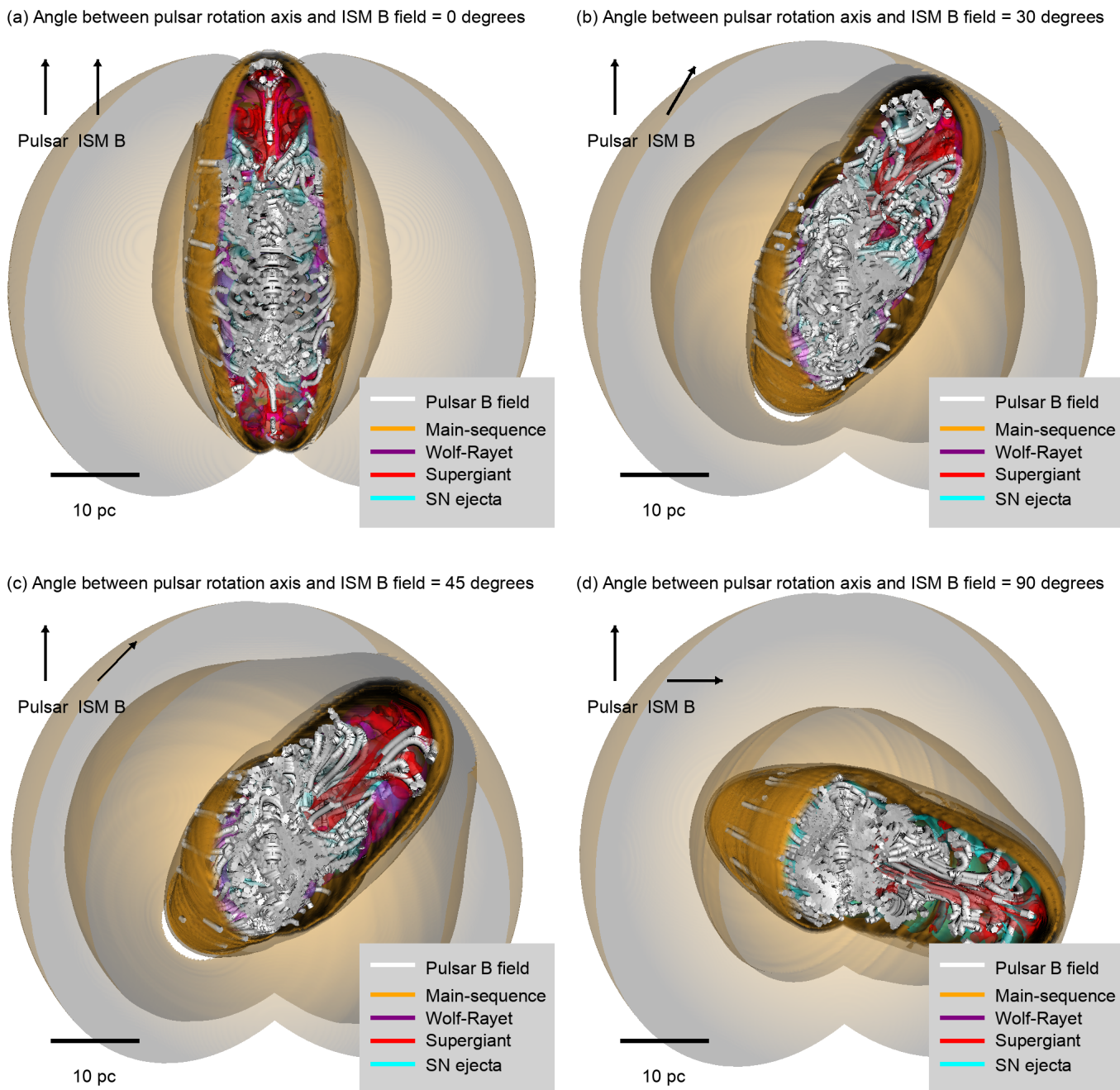


Fig. 3. Rendering of the 3D MHD pulsar wind nebulae and their complex environments. The orange surfaces trace constant density regions of the stellar wind bubble, the red surfaces trace the red supergiant wind, the magenta surface trace the Wolf-Rayet wind, the cyan surface traces the supernova ejecta and the white tubes trace the magnetic field in the pulsar wind. The 3D figures are clipped with two planes permitting a visualization of the internal structure of the plerionic supernova remnant. The displayed models differ only by the angle between the ISM magnetic field lines that shape the main-sequence stellar wind bubble (orange) and the axis of rotation of the pulsar (fixed in all models as being along the vertical direction). The angle is of $\theta_{\text{mag}} = 0^\circ$ (a), $\theta_{\text{mag}} = 30^\circ$ (b), $\theta_{\text{mag}} = 45^\circ$ (c) and $\theta_{\text{mag}} = 90^\circ$ (d), respectively.

model; second, the incomplete treatment of microphysical processes included in the simulations; and third, the static nature of the pulsar. Let us discuss these points in more detail.

The 2.5D magnetohydrodynamical simulations of the circumstellar medium require models in which the motion of the progenitor star aligns with the direction of the ISM magnetic field. A fully 3D representation of the stellar environment during the pre-supernova phase (Geen et al. 2015) would overcome this constraint and improve the accuracy of the modeled plerions,

particularly regarding the interaction of the supernova blast wave with the walls of the stellar cavity. A desired improvement, today numerically unreachable, would be to consider this problem in the frame of relativistic magneto-hydrodynamics, addressing amongst others, the effects of the adiabatic index on the structure and emission properties of plerionic supernova remnants. In addition, relativistic effects, principally relevant for the emission of the inner pulsar wind nebula such as the Doppler boosting or emission aberration are not included yet in the construction

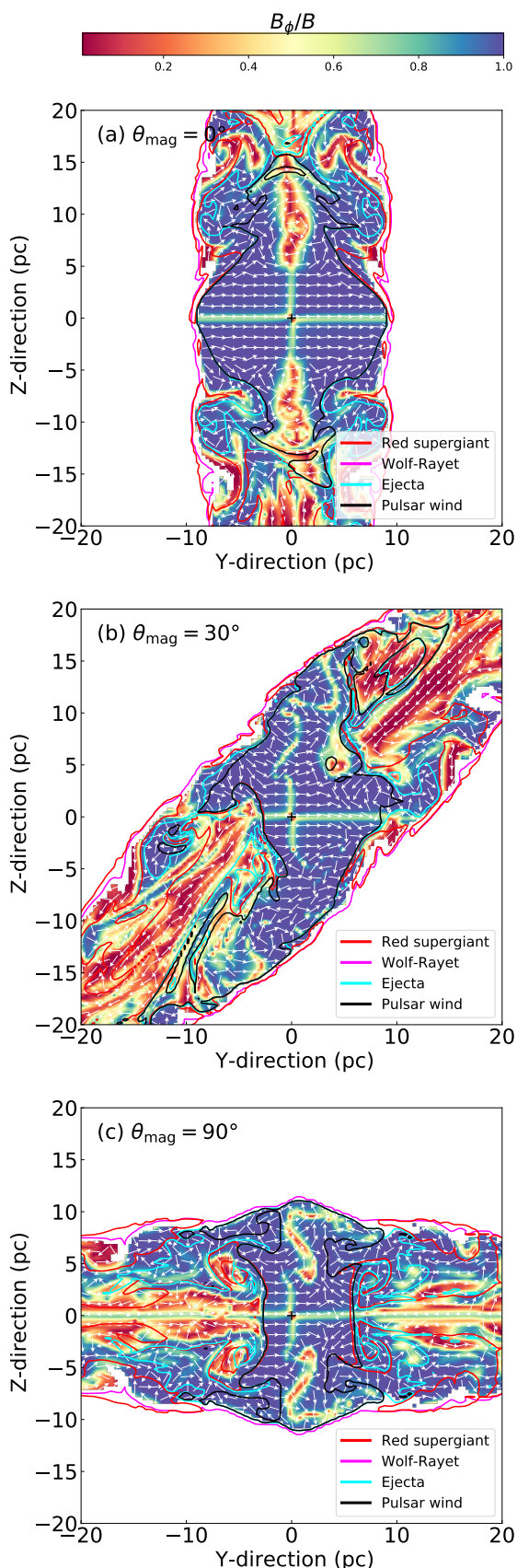


Fig. 4. Distribution of the toroidal to total magnetic field ratio B_ϕ/B in the 3D supernova remnant models. The white arrows trace the magnetic field in the yOz plane for the region of the supernova remnant. The figures show the supernova remnants in the $x = 0$ plane of the Cartesian coordinate system, at time 70 kyr after the onset of the explosion.

of the synchrotron maps. This can alter the apparent distribution of the projected emission in the polar elongation/torus regions and therefore limits direct one-to-one comparison to real high-resolution pulsar wind nebula images, which are out of the scope of this study.

Although our models incorporate magnetic fields along with optically thin radiative cooling and heating, other physical mechanisms, such as electron heat conduction or non-ideal magnetohydrodynamical effects, are neglected and should ideally be considered in future studies. Thermal conduction will smooth discontinuities and transitions in the density and the temperature fields, in particular at the termination shocks and inside of the hot layers of low-density material (Balsara et al. 2008; Meyer et al. 2014), the latter will add realism to the local magnetic field properties and its effects on the growth of dust grains (Gutiérrez-Vera et al. 2023; Giang & Hoang 2024).

The pulsar considered in our simulations is static and does not move relative to the progenitor star; that is, the natal kick imparted during the supernova explosion is not accounted for. However, pulsars typically receive kick velocities of several hundred m s^{-1} (Verbunt et al. 2017), which can displace them by up to 10 pc within the supernova remnant (Igoshev 2020; Igoshev et al. 2020). Given the size of the cavity carved by the progenitor in the ISM, a moving pulsar would still remain within it, and would thus have only a second-order effect on the overall morphology of the pulsar wind nebula (Meyer et al. 2024a). The star itself, but also the local inhomogeneities of the ISM, also influence the emission of the pulsar wind nebula, via their control onto the circumstellar distribution of material at the pre-supernova time. They constitute a vast parameter space needs to be explored. All these factors (Fig. D.1) could enhance the realism of the simulations, and, in turn, improve the accuracy of the resulting synthetic emission maps when compared with real observations.

4.2. Synchrotron maps

Fig. 6 displays synchrotron 1.4 GHz radio emission maps of the model with $\theta_{\text{mag}} = 0^\circ$ at 80 kyr, as seen from different angles defined by the observer’s inclination θ_{incl} (between the line of sight and the projection plane of the supernova remnant) and an azimuthal angle ϕ . The panel with $\theta_{\text{incl}} = 0^\circ$ and $\phi = 0^\circ$ shows the overall shape of the stellar wind cavity. The termination shock appears brightest at the end of the cavity and forms a thick ring around the center of the explosion (Fig. 6a). This feature is described in the 2.5-dimensional context in Meyer et al. (2024a). Our 3D treatment of the pulsar wind nebula phase reveals non-axisymmetric features in the reverberated termination shock, producing a north–south asymmetry relative to the pulsar’s rotational plane, as well as east–west irregularities. Fig. 6b shows the same plerion viewed at $\theta_{\text{incl}} = 45^\circ$ and $\phi = 0^\circ$. A rectangular morphology is visible, consistent with earlier findings for core-collapse supernova remnants of a $35 M_\odot$ star (van Marle et al. 2015; Meyer et al. 2022), and for the plerionic case specifically in Meyer et al. (2024a). In our model, a similar rectangular shape is observed, with a southern bright extension produced by the polar elongation penetrating into the lower part of the cavity. The final panel, with $\theta_{\text{incl}} = 90^\circ$ and $\phi = 0^\circ$, shows the plerionic core-collapse supernova remnant as a roughly circular structure—an effect of the 2.5-dimensional nature of the circumstellar medium (Fig. 6c).

Fig. E.1a displays the emission maps of the simulation with $\theta_{\text{mag}} = 30^\circ$, viewed with $\theta_{\text{incl}} = 0^\circ$ and $\phi = 0^\circ$. The peculiar shape of the cavity into which the pulsar wind is channeled

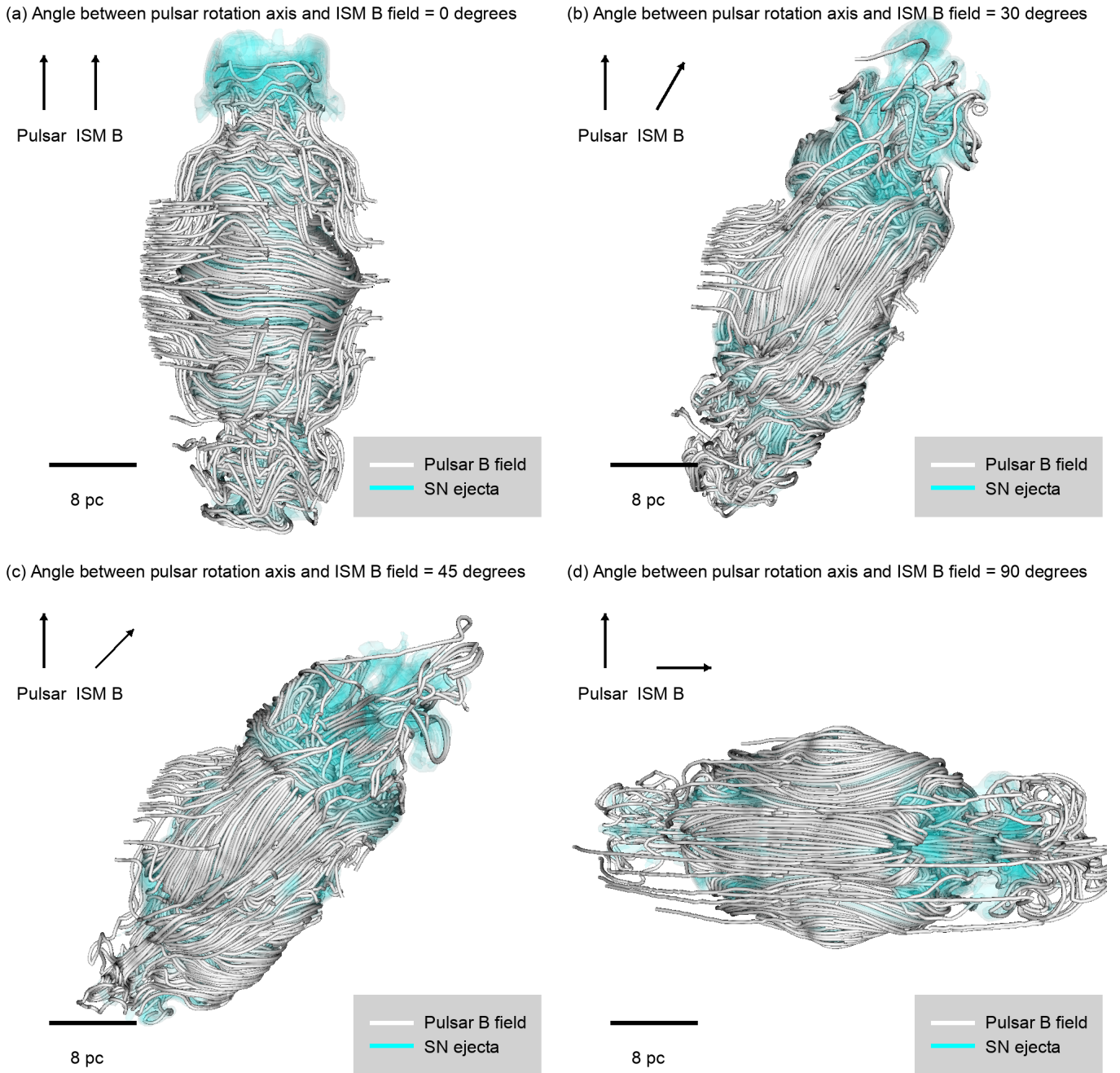


Fig. 5. Same as Fig. 3, displaying the 3D magnetic field distribution of the pulsar wind nebulae within the supernova ejecta. It highlights how the supernova ejecta distribution (itself governed by the circumstellar medium and the magnetization of the ISM) influences the manner the propagation of the pulsar wind and the arrangement of its magnetic field lines. An animated version of this figure is available as online material.

does not produce a rectangular morphology; instead, it results in an oblong or ovoidal structure that is broader in the northern region and narrower in the southern region, with an equatorial ring formed by the pulsar wind disc. This ring is not visible at $\theta_{\text{incl}} = 45^\circ$ and $\phi = 0^\circ$, while the north–south asymmetries in the projected emission become more pronounced, further emphasizing the difference in thickness of the pulsar wind nebula’s termination shock (Fig. E.1b). At $\theta_{\text{incl}} = 90^\circ$ and $\phi = 0^\circ$, the equatorial bulge generated by the ring reappears at the center of a cross-shaped morphology of the stellar wind cavity (Fig. E.1c). In the case of $\theta_{\text{mag}} = 45^\circ$, the pulsar wind nebula is seen inside the cavity with a distinct equatorial ring and polar elongation,

again exhibiting north–south asymmetries due to the fully 3D nature of the simulation (Fig. E.2a, b, c). For $\theta_{\text{mag}} = 90^\circ$, the situation is similar, except that the projected pulsar wind appears more compact at $\theta_{\text{incl}} = 0^\circ$ and $\phi = 0^\circ$ compared to the projections at $\theta_{\text{incl}} = 45^\circ$ or $\theta_{\text{incl}} = 90^\circ$ with $\phi = 0^\circ$ (see Fig. E.3a, b, c).

4.3. Mixing of materials

Fig. 9 shows the mixing of various materials in the plerionic supernova remnant at time 80 kyr after the supernova explosion. The line colors indicate the mixing of material from the main-sequence (orange), red supergiant (red), Wolf–Rayet (magenta)

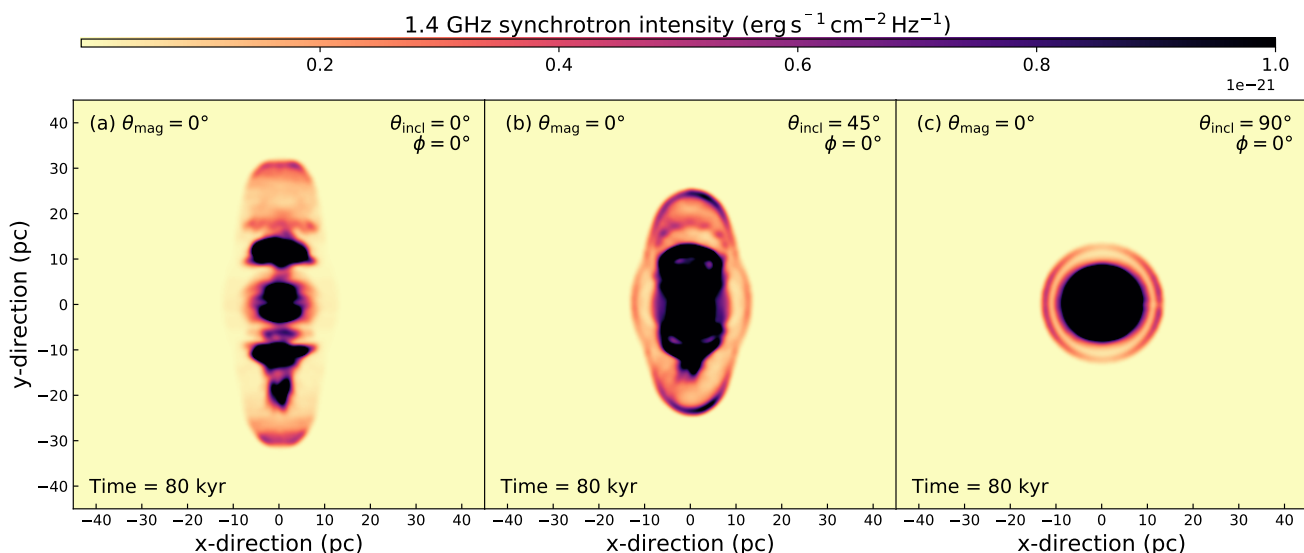


Fig. 6. Synchrotron 1.4 GHz radio emission maps of the model with $\theta_{\text{mag}} = 0^\circ$ at times 80 kyr as seen with an angle between the observers point of view and the plan in which the supernova remnant is projected $\theta_{\text{incl}} = 0^\circ$.

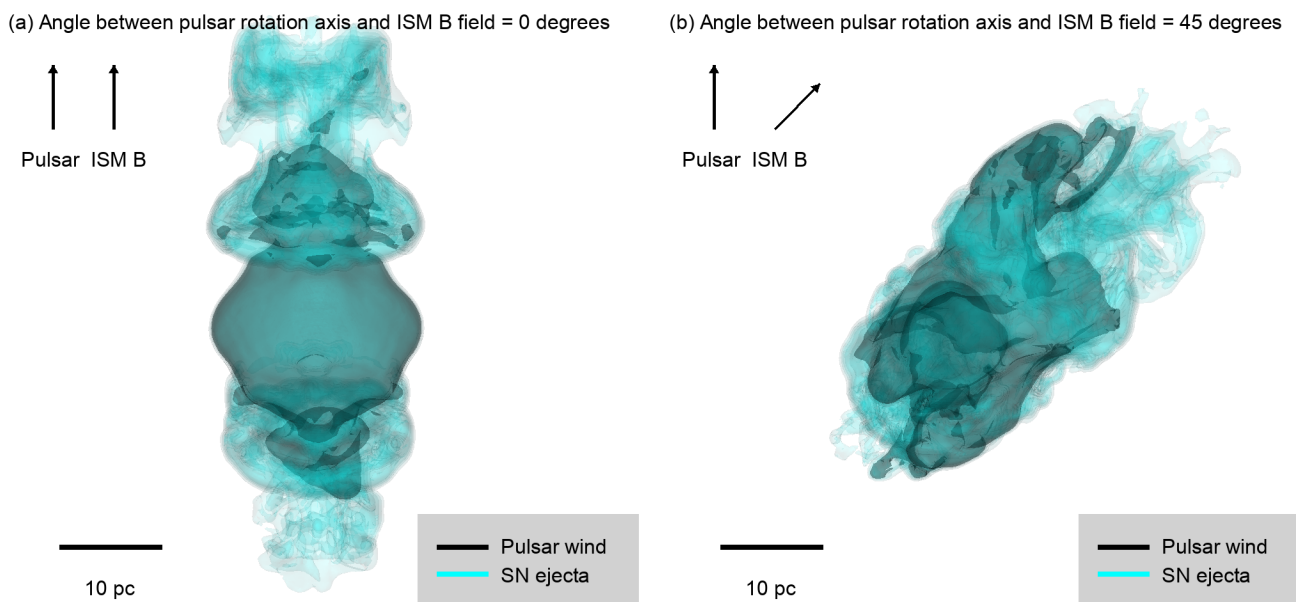


Fig. 7. Same as Fig. 3, displaying the contact discontinuity of the pulsar wind material (50% in number density) within the surrounding supernova ejecta (cyan) at time 80 kyr with $\theta_{\text{mag}} = 0^\circ$ (a) and $\theta_{\text{mag}} = 45^\circ$ (b). The figure shows plerion at an advance age of their evolution, when the deviation exerted by the circumstellar medium onto the morphology of the pulsar wind nebula is maximum. An animated version of this figure is available as online material.

winds, supernova ejecta (cyan), and pulsar wind (black), respectively, plotted as a function of the angle θ_{mag} between the ISM magnetic field and the pulsar’s rotation axis. The mixing is considered at later times in this study, because we aim at extracting conclusions for quasi-steady situations. Before the forward shock of the supernova blastwave hits the walls of the cavity and meets the expanding pulsar wind, the plerion is essentially growing symmetrically, without any influence from its progenitor’s circumstellar medium, as described in (Meyer & Torres 2025).

The mixing efficiency is calculated using passive tracers for each material (main-sequence, red supergiant, and Wolf–Rayet winds, supernova ejecta, and pulsar wind), as well as the mass density and gas velocity. These quantities allow for the tracking

of advection from the inner boundary, where winds and ejecta are injected, throughout the supernova remnant, as employed in previous studies (Orlando et al. 2005). Efficiency is defined as the ratio of the mass of a given component within the volume of the remnant to the total mass of the remnant. The spatial extent of the remnant is identified from the computational domain using a threshold in the density of the unperturbed ISM number. The figure demonstrates that, at 80 kyr after the explosion, the differences in θ_{mag} (the angle between the ISM magnetic field and pulsar spin axis) do not fundamentally alter the global mixing within the cavity. By this time, the supernova blastwave has had sufficient time to traverse the cavity repeatedly, driven by the continuously injected pulsar wind.

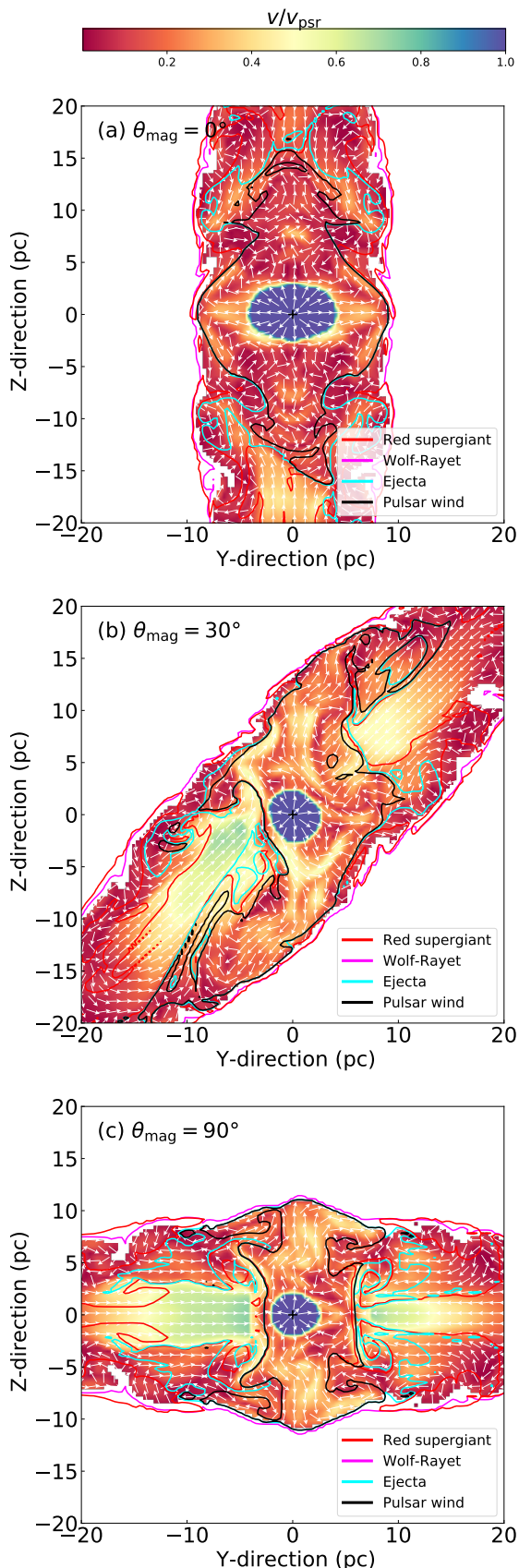


Fig. 8. Distribution of the velocity field in the 3D supernova remnant models, plotted in units of the pulsar wind velocity v_{psr} . The white arrows trace the velocity field in the yOz plane. The figures show the supernova remnants in the $x = 0$ plane of the Cartesian coordinate system, at time 70 kyr after the onset of the explosion.

The mixing efficiency approaches 100% for both main-sequence and Wolf-Rayet materials. This can be attributed to two main factors: (i) the large-scale stellar wind bubble beyond the cavity predominantly contains shocked ISM material due to the absence of electronic heat conduction in our magnetized circumstellar nebula models (Meyer et al. 2017, 2015), and (ii) all remaining main-sequence gas within the cavity has been multiply shocked by successive phases of the evolved winds, the supernova ejecta, and the pulsar wind. The Wolf-Rayet wind is also highly mixed, as it is the first material encountered by both the blastwave and the pulsar wind. In contrast, the red supergiant wind, supernova ejecta, and pulsar wind exhibit each a mixing efficiency of approximately 20%, suggesting a degree of material preservation. This indicates the relative purity of the red supergiant wind - rich in hot H-burning products - as well as of the inner remnant material containing Mg, Si, Ca, Ti, and Fe originating from explosive nucleosynthesis in the supernova and pulsar wind nebulae. The quantity and density of materials are different, as well as the time they are exposed to other materials. The Wolf-Rayet material is present in smaller quantity and is directly shocked by the supernova blastwave. The main-sequence material is successively shocked by all materials since the onset of the explosion, while supernova ejecta and pulsar wind interact directly. These findings are consistent with 2D simulations presented in Meyer & Torres (2025), which examined the mixing of these same species during the first 9 kyr of the supernova remnant's evolution inside a stellar wind bow shock.

4.4. Bending of the polar elongations by the progenitor past stellar wind history

Fig. 7 plots the isosurface of the tracer for the pulsar wind material at 50% number density in the simulation with $\theta_{\text{mag}} = 0^\circ$ (Fig. 7a) and with $\theta_{\text{mag}} = 45^\circ$ (Fig. 7b), respectively. The volume rendering reveals how the pulsar wind is channeled into the inner region of the circumstellar medium of the progenitor star. When the rotation axis of the pulsar is aligned with the local ISM magnetic field direction, the pulsar wind nebula grows with the typical morphology of an equatorial disc and a polar elongation, which is itself affected by instabilities. In the case with an angle $\theta_{\text{mag}} = 45^\circ$, the direction of the stellar wind cavity and the direction along which the polar elongation develops is tilted by an angle approximately equal to $\theta_{\text{mag}} = 45^\circ$.

Our results therefore demonstrate a new mechanism to explain how the polar elongations of the pulsar wind nebula grow and become unstable. Specifically, the bending of the tails of a pulsar wind nebula, which are subject to kink instabilities that self-consistently disturb the polar elongation, has been shown to produce helical polar elongation deformations (Mignone et al. 2010). Our findings show that the circumstellar medium of the supernova progenitor plays a critical role in shaping the pulsar wind nebula and determining its emission properties, as previously demonstrated in the context of static massive stars with a pulsar rotation axis aligned with the local ISM magnetic field (Meyer et al. 2024c), and in the context of runaway pulsars moving through a Cygnus-loop-type supernova remnant created by a runaway red supergiant-evolving progenitor (Meyer et al. 2025). Fig. 8 further highlights the velocity field in the yOz plane of the supernova remnants a time 70 kyr, which is radial inside the free-streaming wind region, organised within the disc-like region of the unmixed pulsar wind nebula (black contour), and more disorganised in the polar regions of it. Fast bouncing material move from the edge of the cavity towards the pulsar wind

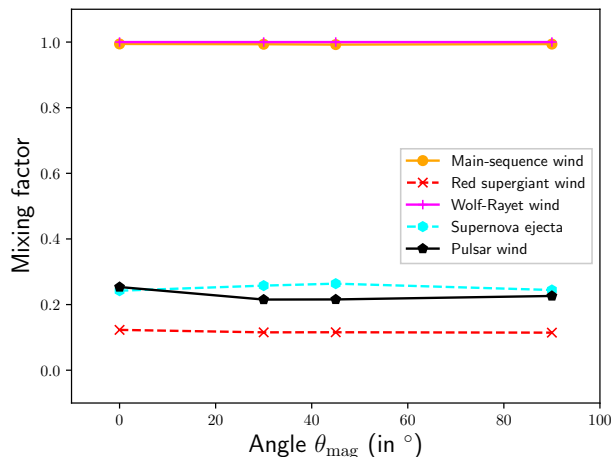


Fig. 9. Mixing of the different materials in the plerionic supernova remnant at time 80 kyr after the supernova explosion. The line colours distinguish the mixing for the main-sequence (orange), red supergiant (red), Wolf-Rayet (magenta) wind materials, supernova ejecta (cyan), and pulsar wind (black), respectively, displayed as a function of the angle θ_{mag} between the ISM magnetic field and the rotation axis of the pulsar.

nebula, imposing its bipolar flow to shape as twisted extensions (Fig. 8b).

5. Conclusion

This study investigates the influence of the inclination angle between the direction of the ISM magnetic field and the rotational axis of the pulsar formed at the explosion site of a rotating, magnetized, massive progenitor star with an initial mass of $M_{\star} = 35 M_{\odot}$. The primary objective is to determine how this angular configuration affects the morphology of non-thermal radio emission maps produced by synchrotron radiation within the expanding supernova remnant. The numerical models employed track the dynamical evolution of the supernova blastwave as it propagates through the circumstellar medium of the progenitor star, extending up to 35 kyr after the core-collapse event.

To perform these simulations, the circumstellar medium is initially computed using 2.5D magnetohydrodynamic simulations, which model the stellar evolution from the zero-age main-sequence phase to the pre-supernova stage. These models incorporate the effects of stellar mass loss through winds and the evolution of the large-scale magnetic field in the surrounding environment. The interaction between the supernova blastwave and the circumstellar medium is modeled in a multi-step approach, beginning with 1D simulations that track the formation and expansion of the supernova shock wave as it propagates through the stellar wind. These calculations provide insight into the radial structure of the blastwave and the development of shocked regions in the circumstellar medium. The subsequent large-scale expansion of the supernova remnant is computed within a fully 3D Cartesian numerical framework, allowing for the inclusion of asymmetries introduced by the interstellar medium's magnetic field and the anisotropic distribution of supernova ejecta. To assess the observational implications of these simulations, synchrotron radiation emission maps at radio wavelengths are generated.

Following the study of Meyer et al. (2024c) and Meyer et al. (2025), we found that the circumstellar medium of the massive

progenitor governs the morphology and the emission properties of the pulsar wind nebulae. In this series of simulations, the free parameter is the angle between the rotation axis of the pulsar and the local direction of the ISM magnetic field, which determines the direction of the cavity formed by the stellar wind during the evolutionary history of the massive star. In particular, we found that this angle can channel the polar elongation of the pulsar wind along directions that are not perpendicular to the disc of the pulsar wind nebula, offering an alternative explanation to the kink instabilities previously invoked to explain the ragged and irregular appearance of these polar elongation as they propagate through the complex region of evolved stellar winds, supernova ejecta, and pulsar wind material.

Emission maps for the synchrotron 1.4 GHz radio waveband reveal a wide variety of shapes, combining the projection of the dense, magnetized post-shock region of the stellar cavity impacted by the supernova remnant with the projection of the emission generated by the pulsar wind material within it. This results in a vast range of morphologies, spanning from rectangular to circular forms, as well as more irregular structures exhibiting north-south and east-west asymmetries. The results show that, at the advanced age of the supernova remnants considered, the angle between the ISM magnetic field and the pulsar rotation axis does not significantly affect the mixing of material within the system.

Acknowledgements. The authors acknowledge RES resources provided by BSC in MareNostrum to AECT-2025-1-0004. The authors also acknowledge computing time on the high-performance computer "Lise" at the NHR Center NHR@ZIB. This center is jointly supported by the Federal Ministry of Education and Research and the state governments participating in the NHR (www.nhr-verein.de/unsere-partner). This work has been supported by the grant PID2024-155316NB-I00 funded by MICIU/AEI/10.13039/501100011033/FEDER, UE, IIEC APEC2043, and CSIC PIE 202350E189. This work was also supported by the Spanish program Unidad de Excelencia María de Maeztu CEX2020-001058-M and also supported by MCIN with funding from European Union NextGeneration EU (PRTR-C17.11).

References

- Abdalla, H., Aharonian, F., Ait Benkhali, F., et al. 2021, *ApJ*, 917, 6
- Acero, F., Acharyya, A., Adam, R., et al. 2023, *Astroparticle Physics*, 150, 102850
- Aharonian, F., Akhperjanian, A. G., Bazer-Bachi, A. R., et al. 2006, *A&A*, 457, 899
- Asplund, M., Grevesse, N., Sauval, A. J., & Scott, P. 2009, *ARA&A*, 47, 481
- Baalmann, L. R., Scherer, K., Fichtner, H., et al. 2020, *A&A*, 634, A67
- Baalmann, L. R., Scherer, K., Kleimann, J., et al. 2021, *A&A*, 650, A36
- Balsara, D. S., Tilley, D. A., & Howk, J. C. 2008, *MNRAS*, 386, 627
- Barkov, M. V. & Bosch-Ramon, V. 2018, *MNRAS*, 479, 1320
- Barkov, M. V., Lyutikov, M., & Khangulyan, D. 2019a, *MNRAS*, 484, 4760
- Barkov, M. V., Lyutikov, M., Klingler, N., & Bordas, P. 2019b, *MNRAS*, 485, 2041
- Begelman, M. C. 1998, *ApJ*, 493, 291
- Begelman, M. C. & Li, Z.-Y. 1992, *ApJ*, 397, 187
- Bock, D. C. J., Turtle, A. J., & Green, A. J. 1998, *AJ*, 116, 1886
- Borkowski, K. J., Reynolds, S. P., & Roberts, M. S. E. 2016, *ApJ*, 819, 160
- Bucciantini, N. 2018, *MNRAS*, 478, 2074
- Bucciantini, N. & Bandiera, R. 2001, *A&A*, 375, 1032
- Bucciantini, N., Bandiera, R., Blondin, J. M., Amato, E., & Del Zanna, L. 2004, *A&A*, 422, 609
- Bühler, R. & Blandford, R. 2014, *Reports on Progress in Physics*, 77, 066901
- Camus, N. F., Komissarov, S. S., Bucciantini, N., & Hughes, P. A. 2009, *MNRAS*, 400, 1241
- Castro, N., Fossati, L., Hubrig, S., et al. 2015, *A&A*, 581, A81
- Caswell, J. L. 1979, *MNRAS*, 187, 431
- Chevalier, R. A. & Luo, D. 1994, *ApJ*, 421, 225
- Coroniti, F. V. 1990, *ApJ*, 349, 538
- de Wit, W. J., Testi, L., Palla, F., & Zinnecker, H. 2005, *A&A*, 437, 247
- Decin, L., N. L. J., Royer, P., et al. 2012, *A&A*, 548, A113
- Del Zanna, L., Amato, E., & Bucciantini, N. 2004, *A&A*, 421, 1063
- Del Zanna, L., Volpi, D., Amato, E., & Bucciantini, N. 2006, *A&A*, 453, 621

- Drissen, L. N., Domček, V., Vink, J., et al. 2018, *ApJ*, 860, 133
- Dullemond, C. P. 2012, *RADMC-3D: A multi-purpose radiative transfer tool*, Astrophysics Source Code Library
- Ekström, S., Georgy, C., Eggenberger, P., et al. 2012, *A&A*, 537, A146
- Eldridge, J. J., Genet, F., Daigne, F., & Mochkovitch, R. 2006, *MNRAS*, 367, 186
- Fossati, L., Castro, N., Morel, T., et al. 2015, *A&A*, 574, A20
- Frail, D. A. & Scharringhausen, B. R. 1997, *ApJ*, 480, 364
- Gaensler, B. M. & Slane, P. O. 2006, *ARA&A*, 44, 17
- Geen, S., Rosdahl, J., Blaizot, J., Devriendt, J., & Slyz, A. 2015, *MNRAS*, 448, 3248
- Giang, N. C. & Hoang, T. 2024, *MNRAS*, 530, 984
- Gold, T. 1968, *Nature*, 218, 731
- González, R. F. & Koenigsberger, G. 2014, *A&A*, 561, A105
- Gull, T. R. & Sofia, S. 1979, *ApJ*, 230, 782
- Gutiérrez-Vera, N., Grassi, T., Bovino, S., et al. 2023, *A&A*, 670, A38
- H. E. S. S. Collaboration, Abdalla, H., Abramowski, A., et al. 2018, *A&A*, 612, A2
- H. E. S. S. Collaboration, Abdalla, H., Aharonian, F., et al. 2019, *A&A*, 627, A100
- Harten, A., Lax, P. D., & van Leer, B. 1983, *SIAM Review*, 25, 35
- Henney, W. J., Arthur, S. J., de Colle, F., & Mellema, G. 2009, *MNRAS*, 398, 157
- Herbst, K., Scherer, K., Ferreira, S. E. S., et al. 2020, *ApJ*, 897, L27
- Hester, J. J. 2008, *ARA&A*, 46, 127
- Hummer, D. G. 1994, *MNRAS*, 268, 109
- Igoshev, A. P. 2020, *MNRAS*, 494, 3663
- Igoshev, A. P., Perets, H. B., & Michaely, E. 2020, *MNRAS*, 494, 1448
- Kargaltsev, O., Durant, M., Pavlov, G. G., & Garmire, G. 2012, *ApJS*, 201, 37
- Kargaltsev, O. & Pavlov, G. 2007, *Ap&SS*, 308, 287
- Kargaltsev, O., Pavlov, G. G., Klingler, N., & Rangelov, B. 2017a, *Journal of Plasma Physics*, 83, 635830501
- Kargaltsev, O., Pavlov, G. G., Klingler, N., & Rangelov, B. 2017b, *Journal of Plasma Physics*, 83, 635830501
- Kennel, C. F. & Coroniti, F. V. 1984, *ApJ*, 283, 710
- Kolb, C., Blondin, J., Slane, P., & Temim, T. 2017, *ApJ*, 844, 1
- Komissarov, S. S. 2006, *MNRAS*, 367, 19
- Komissarov, S. S. & Lyubarsky, Y. E. 2003, *MNRAS*, 344, L93
- Komissarov, S. S. & Lyubarsky, Y. E. 2004, *MNRAS*, 349, 779
- Komissarov, S. S. & Lyutikov, M. 2011, *MNRAS*, 414, 2017
- Langer, N. 2012, *ARA&A*, 50, 107
- Lhaaso Collaboration, Cao, Z., Aharonian, F., et al. 2021, *Science*, 373, 425
- Lyne, A. & Graham-Smith, F. 2012, *Pulsar Astronomy*
- McKee, C. F. & Ostriker, J. P. 1977, *ApJ*, 218, 148
- Meyer, D. M. A. 2021, *MNRAS*, 507, 4697
- Meyer, D. M.-A., Langer, N., Mackey, J., Velázquez, P. F., & Gusdorf, A. 2015, *MNRAS*, 450, 3080
- Meyer, D. M.-A., Mackey, J., Langer, N., et al. 2014, *MNRAS*, 444, 2754
- Meyer, D. M. A. & Meliani, Z. 2022, *MNRAS*, 515, L29
- Meyer, D. M. A., Meliani, Z., Velázquez, P. F., Pohl, M., & Torres, D. F. 2024a, *MNRAS*, 527, 5514
- Meyer, D. M. A., Mignone, A., Petrov, M., et al. 2021a, *MNRAS*, 506, 5170
- Meyer, D. M. A., Pohl, M., Petrov, M., & Egberts, K. 2023, *MNRAS*, 521, 5354
- Meyer, D. M. A., Pohl, M., Petrov, M., & Oskinova, L. 2021b, *MNRAS*, 502, 5340
- Meyer, D. M. A. & Torres, D. F. 2025, *MNRAS*, 537, 186
- Meyer, D. M. A., Torres, D. F., & Meliani, Z. 2025, *A&A*, 696, L9
- Meyer, D. M. A., Velázquez, P. F., Petruk, O., et al. 2022, *MNRAS*, 515, 594
- Meyer, D. M. A., Velázquez, P. F., Pohl, M., et al. 2024b, *A&A*, 687, A127
- Meyer, D. M. A., Velázquez, P. F., Pohl, M., et al. 2024c, *A&A*, 687, A127
- Meyer, D. M.-A., Vorobyov, E. I., Kuiper, R., & Kley, W. 2017, *MNRAS*, 464, L90
- Mignone, A., Bodo, G., Massaglia, S., et al. 2007, *ApJS*, 170, 228
- Mignone, A., Rossi, P., Bodo, G., Ferrari, A., & Massaglia, S. 2010, *MNRAS*, 402, 7
- Mignone, A., Zanni, C., Tzeferacos, P., et al. 2012, *ApJS*, 198, 7
- Noriega-Crespo, A., van Buren, D., Cao, Y., & Dgani, R. 1997, *AJ*, 114, 837
- Olimi, B. & Bucciantini, N. 2019a, *MNRAS*, 484, 5755
- Olimi, B. & Bucciantini, N. 2019b, *MNRAS*, 488, 5690
- Olimi, B. & Bucciantini, N. 2019c, *MNRAS*, 490, 3608
- Olimi, B. & Bucciantini, N. 2023, *PASA*, 40, e007
- Olimi, B., Del Zanna, L., Amato, E., Bandiera, R., & Bucciantini, N. 2014, *MNRAS*, 438, 1518
- Olimi, B., Del Zanna, L., Amato, E., Bucciantini, N., & Mignone, A. 2016, *Journal of Plasma Physics*, 82, 635820601
- Orlando, S., Janka, H.-T., Wongwathanarat, A., et al. 2025, *A&A*, 696, A188
- Orlando, S., Miceli, M., Petruk, O., et al. 2019, *A&A*, 622, A73
- Orlando, S., Ono, M., Nagataki, S., et al. 2020, *A&A*, 636, A22
- Orlando, S., Peres, G., Reale, F., et al. 2005, *A&A*, 444, 505
- Orlando, S., Wongwathanarat, A., Janka, H. T., et al. 2022, *A&A*, 666, A2
- Orlando, S., Wongwathanarat, A., Janka, H. T., et al. 2021, *A&A*, 645, A66
- Osterbrock, D. E. & Bochkarev, N. G. 1989, *Soviet Ast.*, 33, 694
- Pacini, F. 1968, *Nature*, 219, 145
- Parker, E. N. 1958, *ApJ*, 128, 664
- Pogorelov, N. V. & Matsuda, T. 2000, *A&A*, 354, 697
- Pogorelov, N. V. & Semenov, A. Y. 1997, *A&A*, 321, 330
- Popov, M. V., Andrianov, A. S., Burgin, M. S., et al. 2019, *Astronomy Reports*, 63, 391
- Porth, O., Komissarov, S. S., & Keppens, R. 2014, *MNRAS*, 438, 278
- Powell, K. G. 1997, *An Approximate Riemann Solver for Magnetohydrodynamics*, ed. M. Y. Hussaini, B. van Leer, & J. Van Rosendale (Berlin, Heidelberg: Springer Berlin Heidelberg), 570–583
- Rand, R. J. & Kulkarni, S. R. 1989, *ApJ*, 343, 760
- Reynolds, S. P., Pavlov, G. G., Kargaltsev, O., et al. 2017, *Space Sci. Rev.*, 207, 175
- Rozyczka, M. & Franco, J. 1996, *ApJ*, 469, L127
- Scherer, K., Baalmann, L. R., Fichtner, H., et al. 2020, *MNRAS*, 493, 4172
- Slane, P. 2017, in *Handbook of Supernovae*, ed. A. W. Alsabti & P. Murdin, 2159
- Temim, T., Slane, P., Kolb, C., et al. 2015, *ApJ*, 808, 100
- Temim, T., Slane, P., Plucinsky, P. P., et al. 2017, *ApJ*, 851, 128
- Temim, T., Slane, P., Raymond, J. C., et al. 2022, *ApJ*, 932, 26
- Toropina, O. D., Romanova, M. M., & Lovelace, R. V. E. 2019, *MNRAS*, 484, 1475
- Tuelove, J. K. & McKee, C. F. 1999, *ApJS*, 120, 299
- Turner, J. D., Stappers, B. W., Carli, E., et al. 2024, *MNRAS*, 531, 3579
- van Buren, D., Noriega-Crespo, A., & Dgani, R. 1995, *AJ*, 110, 2914
- van der Swaluw, E., Achterberg, A., Gallant, Y. A., Downes, T. P., & Keppens, R. 2003, *A&A*, 397, 913
- van der Swaluw, E., Downes, T. P., & Keegan, R. 2004, *A&A*, 420, 937
- van Marle, A. J., Meliani, Z., & Marcowith, A. 2015, *A&A*, 584, A49
- van Veelen, B., Langer, N., Vink, J., García-Segura, G., & van Marle, A. J. 2009, *A&A*, 503, 495
- Verbunt, F., Igoshev, A., & Cator, E. 2017, *A&A*, 608, A57
- Villagran, M. A., Gómez, D. O., Velázquez, P. F., et al. 2024, *MNRAS*, 527, 1601
- Vlemmings, W. H. T., Diamond, P. J., & van Langevelde, H. J. 2002, *A&A*, 394, 589
- Vlemmings, W. H. T., van Langevelde, H. J., & Diamond, P. J. 2005, *A&A*, 434, 1029
- Weaver, R., McCray, R., Castor, J., Shapiro, P., & Moore, R. 1977, *ApJ*, 218, 377
- Weber, E. J. & Davis, Leverett, J. 1967, *ApJ*, 148, 217
- Weiler, K. W. & Panagia, N. 1980, *A&A*, 90, 269
- Weiler, K. W. & Shaver, P. A. 1978, *A&A*, 70, 389
- Whalen, D., van Veelen, B., O’Shea, B. W., & Norman, M. L. 2008, *ApJ*, 682, 49
- Wiersma, R. P. C., Schaye, J., & Smith, B. D. 2009, *MNRAS*, 393, 99
- Wilkin, F. P. 1996, *ApJ*, 459, L31
- Wolfire, M. G., McKee, C. F., Hollenbach, D., & Tielens, A. G. G. M. 2003, *ApJ*, 587, 278

Appendix A: Study concept chart

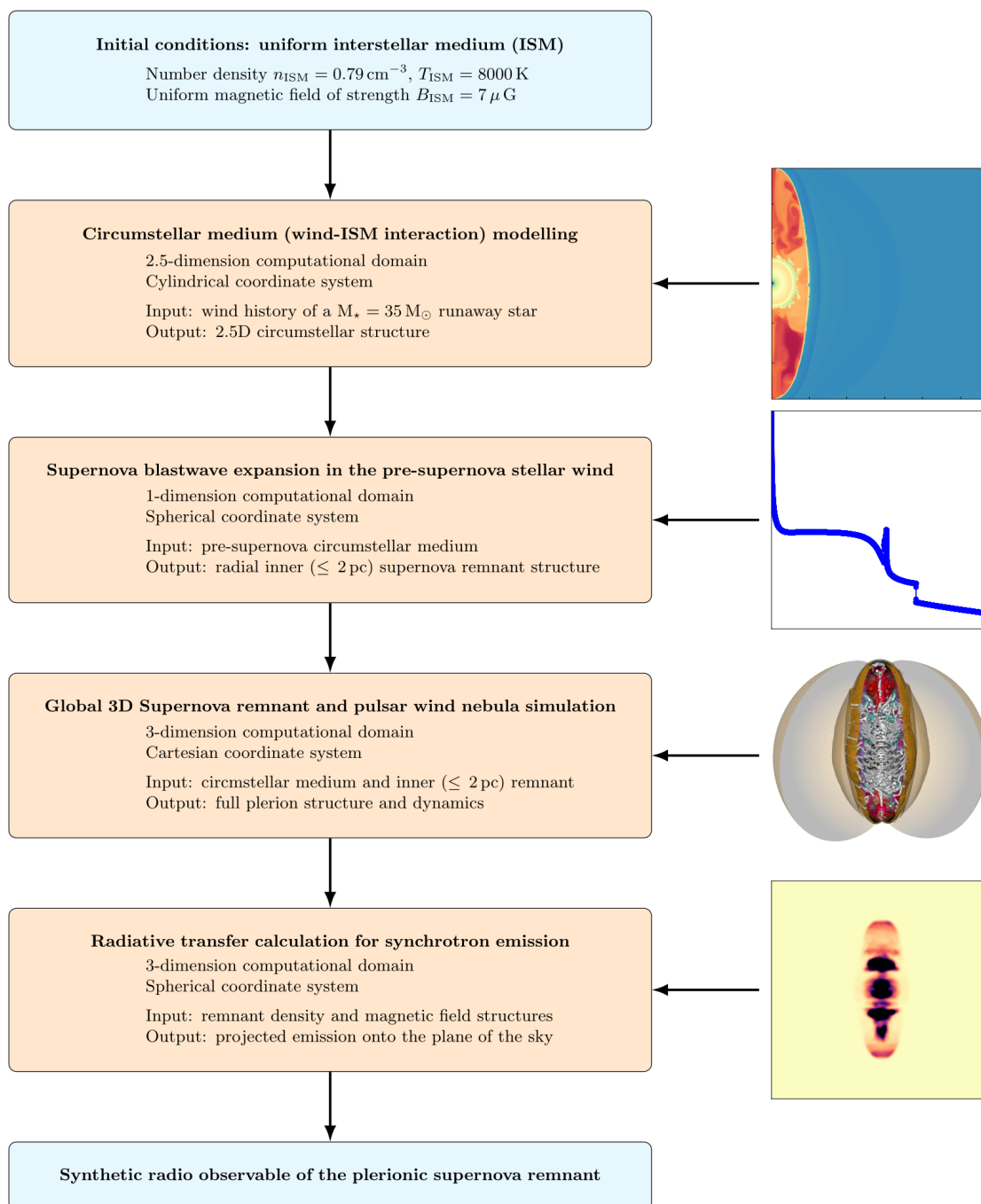


Fig. A.1. Concept chart of the workflow adopted in this study.

Appendix B: Pulsar wind density field at time 50 kyr

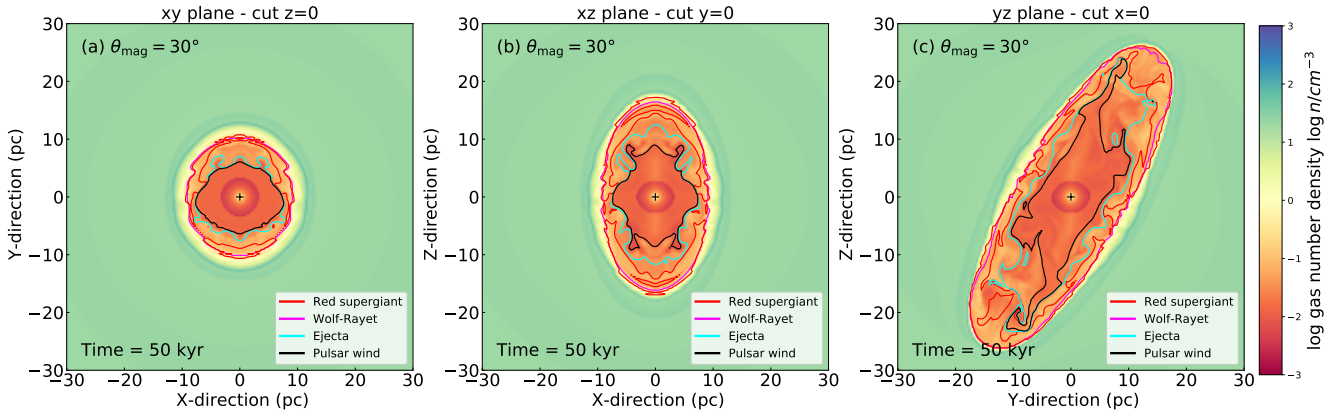


Fig. B.1. Same as Fig. 1 for $\theta_{\text{mag}} = 30^\circ$.

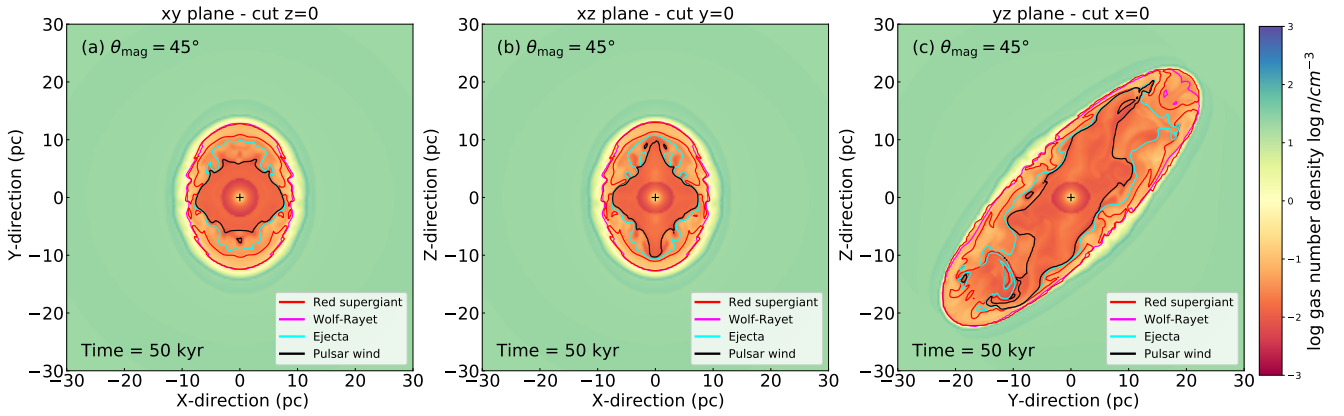


Fig. B.2. Same as Fig. 1 for $\theta_{\text{mag}} = 45^\circ$.

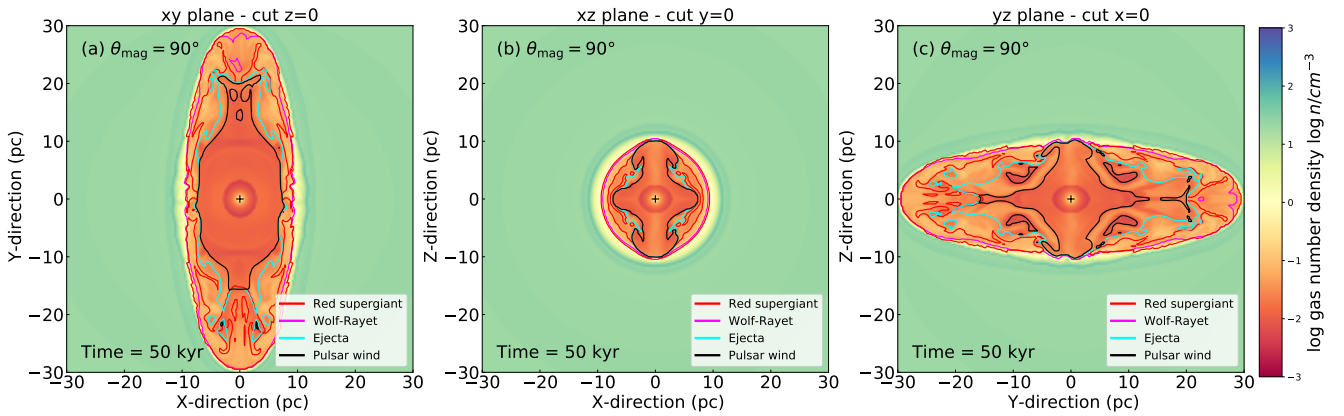


Fig. B.3. Same as Fig. 1 for $\theta_{\text{mag}} = 90^\circ$.

Appendix C: Time evolution of the pulsar wind density field

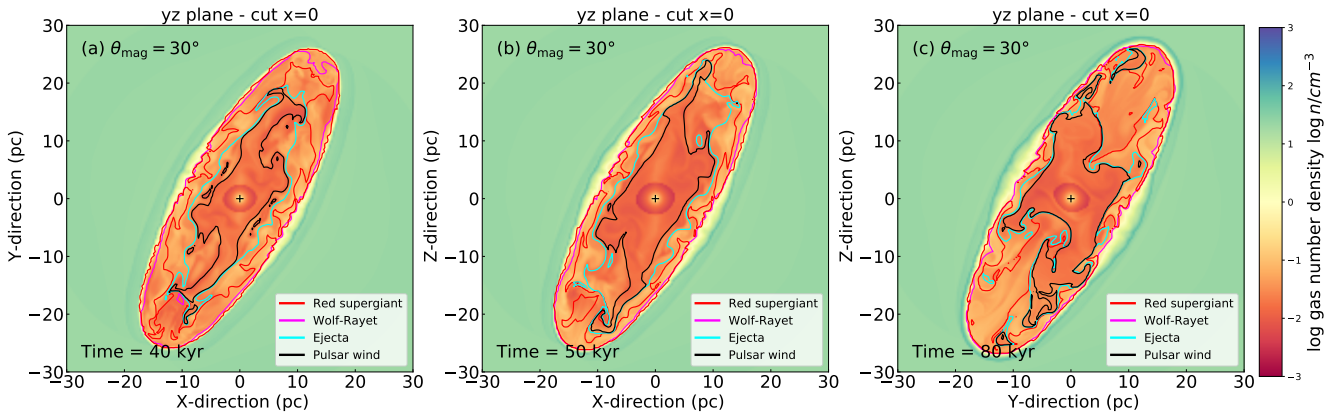


Fig. C.1. Same as Fig. C.1 for $\theta_{\text{mag}} = 30^\circ$.

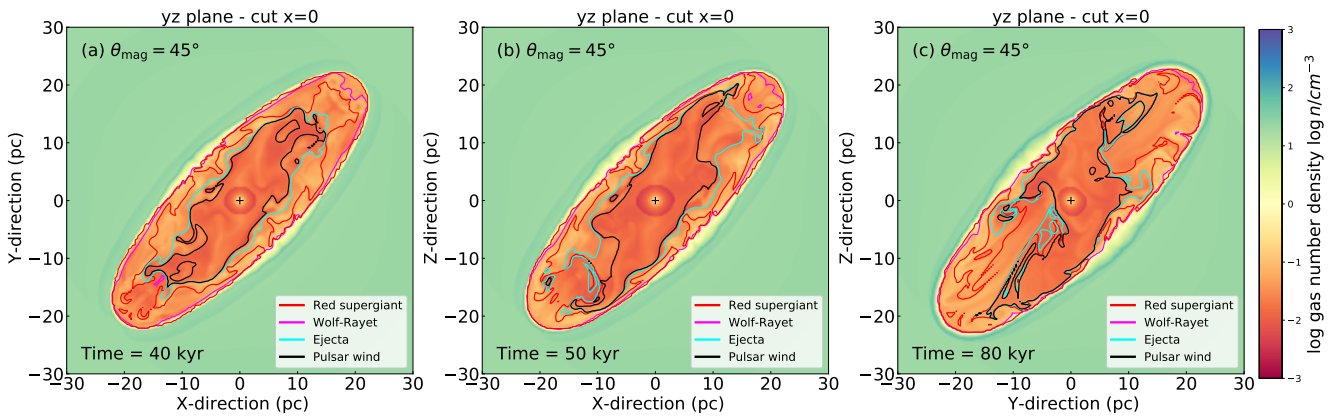


Fig. C.2. Same as Fig. C.2 for $\theta_{\text{mag}} = 45^\circ$.

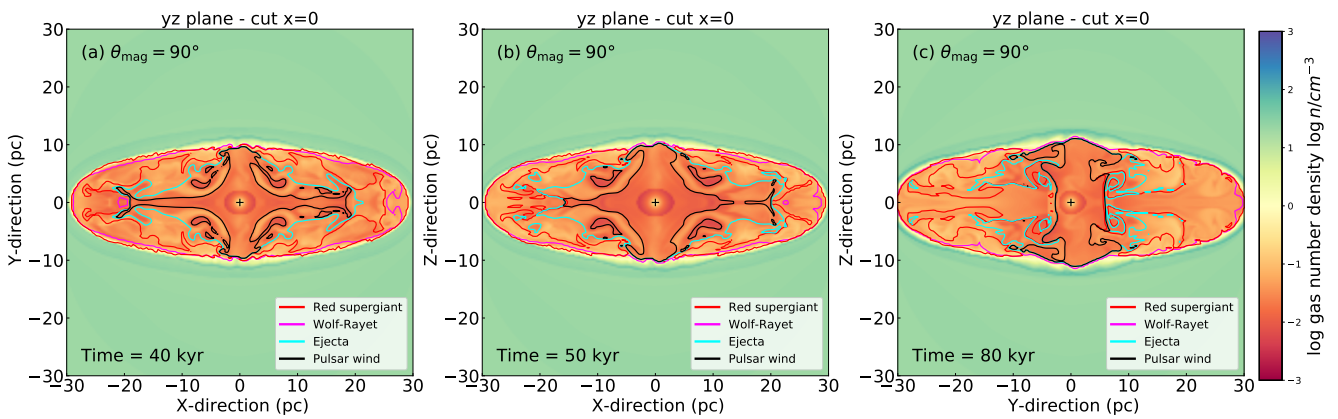
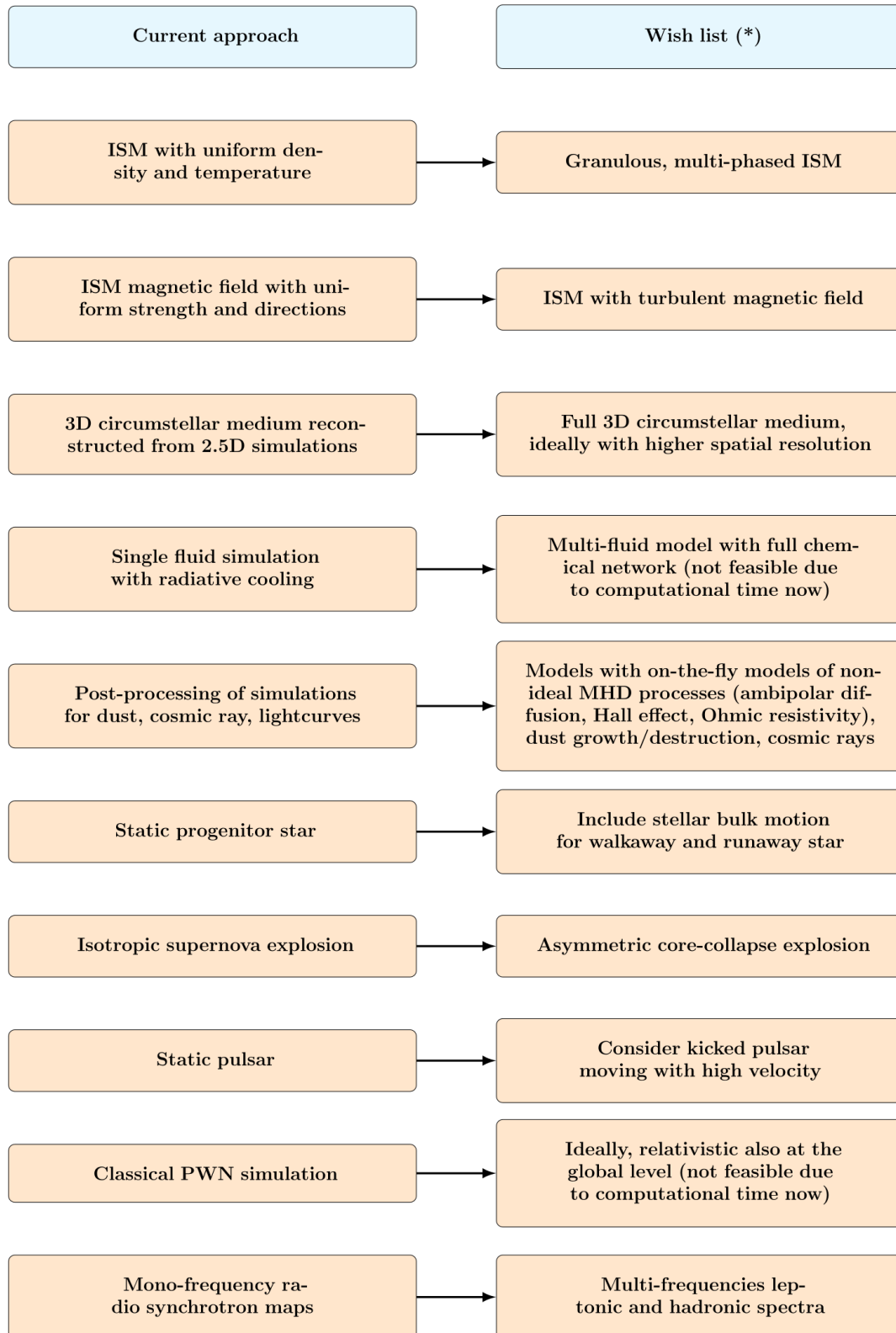


Fig. C.3. Same as Fig. C.3 for $\theta_{\text{mag}} = 90^\circ$.

Appendix D: List of future possible improvements



(*) An effort on simulations with several of those potential updates incorporate is already started 2025arXiv250321492M. We hope to report on that in the near future.

Fig. D.1. Concept chart for future possible improvements of this study.

Appendix E: Emission maps of the pulsar wind nebulae of a static star in a magnetised ISM

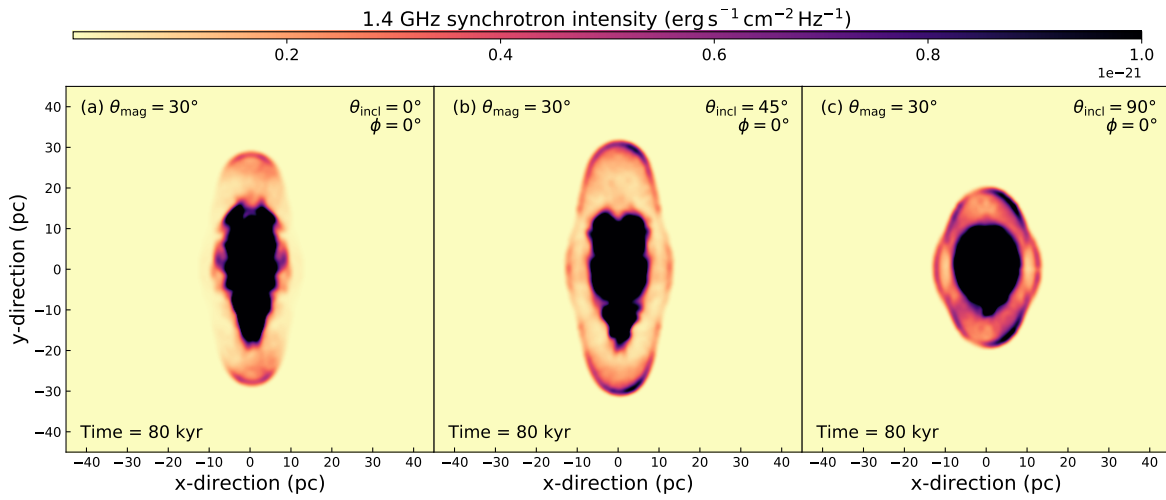


Fig. E.1. Same as Fig. E.1 for $\theta_{\text{incl}} = 30^\circ$.

v

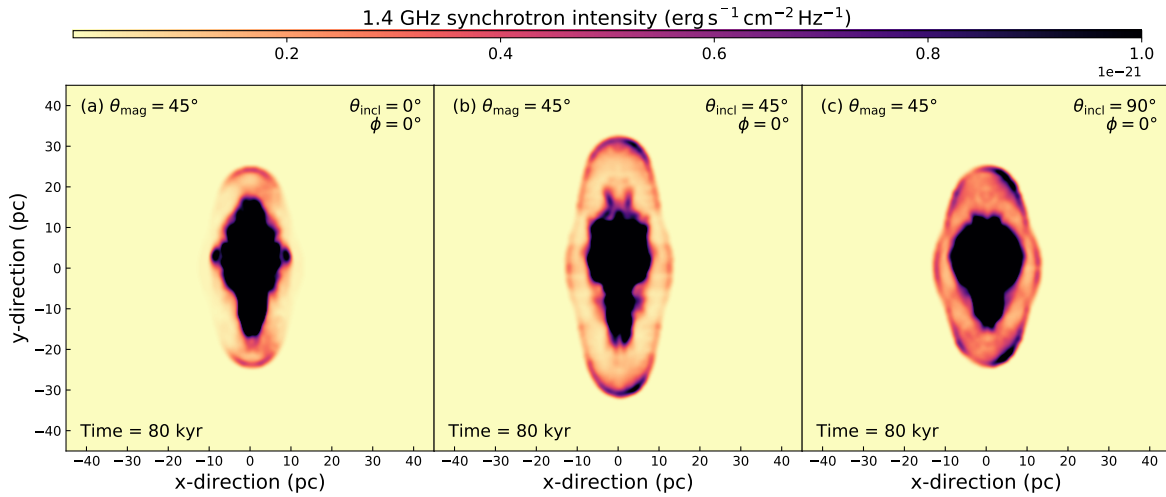


Fig. E.2. Same as Fig. E.1 for $\theta_{\text{incl}} = 45^\circ$.

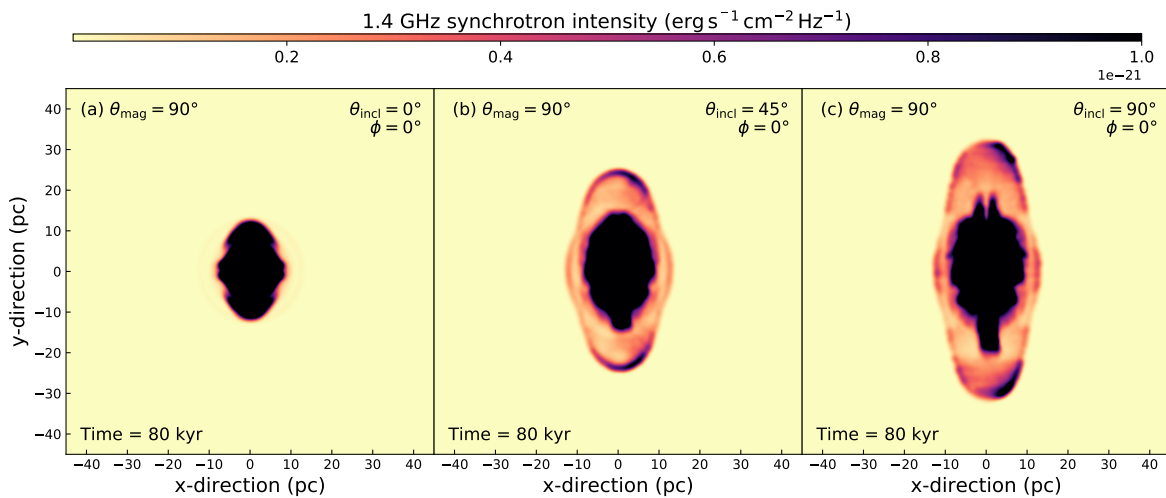


Fig. E.3. Same as Fig. E.1 for $\theta_{\text{incl}} = 90^\circ$.